An adaptive coupling strategy for joint inversions that use petrophysical information as constraints

Björn Heincke[a], Marion Jegen[b], Max Moorkamp[c], Richard W. Hobbs[d], Jin Chen[b]

[a] *GEUS — Geological Survey of Denmark and Greenland,*
Øster Voldgade 10,
DK-1350 Copenhagen, Denmark
E-mail (corresponding author): bhm@geus.dk
[b] *GEOMAR — Helmholtz Centre for Ocean Research,*
Wischhofstrasse 1-3,
[c] *University of Leicester,*
Department of Geology,
Leicester LE1 7RH, United Kingdom
[d] *University of Durham,*
Department of Earth Sciences,
Durham DH1 3LE, United Kingdom

Abstract

Joint inversion strategies for geophysical data have become increasingly popular as they allow for the efficient combination of complementary information from different data sets. The algorithm used for the joint inversion needs to be flexible in its description of the subsurface so as to be able to handle the diverse nature of the data. Hence, joint inversion schemes are needed that 1) adequately balance data from the different methods, 2) have stable convergence behavior, 3) consider the different resolution power of the methods used and 4) link the parameter models in a way that they are suited for a wide range of applications.

Here, we combine active source seismic P-wave tomography, gravity and magnetotelluric (MT) data in a petrophysical joint inversion that accounts

for these issues. Data from the different methods are inverted separately and are linked through constraints accounting for parameter relationships. An advantage of performing the inversions separately is that no relative weighting between the data sets is required. To avoid perturbing the convergence behavior of the inversions by the coupling, the strengths of the constraints are readjusted at each iteration. The criterion we use to control the adaption of the coupling strengths is based on variations in the objective functions from the individual inversions. Adaption of the coupling strengths makes the joint inversion scheme then also applicable to subsurface conditions, where assumed relationships are not valid everywhere, because the individual inversions decouple if it is not possible to reach adequately low data misfits for the made assumptions. The coupling constraints depend on the relative resolutions of the methods, which leads to an improved convergence behavior of the joint inversion compared to a setup, where the resolution is not considered.

Another benefit of the proposed scheme is that structural information can easily be incorporated in the petrophysical joint inversion (no additional terms are added in the objective functions) by using mutually controlled structural weights for the smoothing constraints.

We test our scheme using data generated from a synthetic 2-D sub-basalt model. We observe that the adaption of the coupling strengths makes the convergence of the inversions very robust (data misfits of all methods are close to the target misfits) and that final results are always close to the true models independent of the parameter choices. Finally, the scheme is applied on real data sets from the Faroe-Shetland Basin to image a basaltic sequence

and underlying structures. The presence of a borehole and a 3-D reflection seismic survey in this region allows direct comparison and, hence, evaluate the quality of the joint inversion results. The results from joint inversion are more consistent with results from other studies than the ones from the corresponding individual inversions and the shape of the basaltic sequence is better resolved. However, due to the limited resolution of the individual methods used it was not possible to resolve structures underneath the basalt in detail, indicating that additional geophysical information (e.g. CSEM, reflection onsets) needs to be included.

Keywords: Joint inversion, adaptive coupling, sub-basalt imaging

1. Introduction

Joint inversions are integrated procedures that simultaneously invert data from different geophysical methods. They have become popular in the past decade and there are recent publications about joint inversions in many fields (see Moorkamp et al. (2016) for an overview). Compared to individual inversion of the same datasets resolutions are generally improved and the ambiguities reduced, if the parameters are linked with each other during the inversion stage. The resultant models from joint inversion typically have parameter distributions that are closer to the real distributions of the physical properties in the subsurface, which facilitates subsequent interpretation. However, there are number of problems in joint inversion algorithms; in particular if the involved methods are sensitive to different physical properties (e.g. seismic velocity, density and/or resistivity). This is because:

1. data sets from the individual methods consist of different data types,

sensitivity and numbers of measurements, so their influence on the final model have to be properly balanced during the joint inversion procedure. To find such optimum relative scaling can be difficult and improper scaling results in data from some methods being well-fitted, but data from other methods being seriously under-fitted (or over-fitted);

2. convergence behaviour is often complex and strongly non-linear for some methods (e.g. magnetotelluric, control source electromagnetic, seismic full-waveform tomography) and the convergence path through the model space of each method is typically different. The convergence behaviour and path is further complicated by the coupling within joint inversion. Hence, the joint inversion may get trapped in local minimum far away from an adequate solution where all methods have reasonable data misfits;
3. resolution capabilities of the methods differ and usually vary significantly with location in the model. Like the balance problem in (1) above, ignoring these resolution issues in the joint inversion algorithm may result in a bad data fit for some of the methods, some bias in the models or slow convergence behaviour;
4. assumptions used to link the different methods (or models), typically involve some approximations of the petrophysical or structural relationships that are often not valid for the entire subsurface under investigation. Too rigid implementation of these links or an improper choice of assumptions can result in serious and unpredictable errors in the joint inversion results.

For deterministic approaches that are suitable for handling large number of unknowns and are applicable for problems with time consuming forward calculations, several strategies exist to deal with these problems. To find adequate relative scaling between the data sets (1st problem), most joint inversions algorithms consider only weighting that is defined by the assumed errors of the individual measurements (expressed by the data covariance matrix). Other approaches are purely data driven (e.g. Xu, 2009) or use of multiplicative objective functions to balance the different data sets (e.g. Abubakar et al., 2009). Some inversion approaches (e.g. Günther and Rücker, 2006; Paasche and Tronicke, 2007; Bouchedda et al., 2012; Zhu and Harris, 2015) attempt to overcome this problem by independently inverting the data from different methods and share information from the parameter models between the different inversion runs to promote a similarity between the final models. Such joint inversions are commonly named "cooperative" and have the advantage that no relative weighting between the data sets is required.

To ensure convergence in deterministic inversions (2nd problem), several strategies are proposed that adjust the regularisation strength (Kilmer and O'Leary, 2001; Vogel, 2002) by applying e.g. L-curve fitting (Hansen, 1993), generalized cross-validation (GCV) (Golub and Van Loan, 1996) or the discrepancy principle (Morozov, 1966; Vogel, 2002). For joint inversion e.g. Lelièvre et al. (2012) use a gradually decreasing regularisation that is determined at every iteration from the relationship between the actual data misfit and the specified target misfit. Other joint inversion approaches employ Lagrange multipliers for balancing the coupling constraints that result

in a more stable convergence (e.g. Gallardo and Meju, 2004; Gallardo, 2007).

The impact of resolution power of the individual methods (3rd problem) can be handled by adjusting cell sizes (Lien, 2013) in the parameter models or using independent and spatially flexible regularization strengths for each parameter model.

Structural approaches, which assume that spatial variations in the different parameter models are present at the same locations and are similarly orientated in space, are considered as valid for many subsurface conditions (4th problem) and are widely used (e.g. Haber and Oldenburg, 1997; Gallardo and Meju, 2004; Günther and Rücker, 2006; Doetsch et al., 2010; Molodtsov et al., 2013; Zhu and Harris, 2015). However, there are contributions (e.g. Lelièvre et al., 2012) that note that structural links provide a rather weak coupling resulting only in clear improvements compared to individual inversions in regions that are already relatively well-resolved by most of the individual methods; although other publications (e.g. Moorkamp et al., 2013) show that structural joint inversions can provide superior results even in cases when low-resolution methods are involved. In contrast, other assumptions that are more rigorous and less generally valid, e.g. petrophysical coupling using parameter relationships (Lees and VanDecar, 1991; Afnimar et al., 2002; Moorkamp et al., 2011), often impose a strong coupling and result in significant improvement even for low resolution methods or in parts of the investigated subsurface volume that are not sampled by all of the methods. Which methods work best for a particular joint inversion problem needs to be determined on a case by case basis dependent on the survey design and the geological settings. Some approaches (Colombo

and Stefano, 2007; Lelièvre et al., 2010) have developed options to combine both structural and petrophysical information in the joint inversion. Other joint inversions either use more generally valid assumptions for petrophysical coupling by employing flexible parameter relationships that can be modified during the inversion process (Nielsen and Jacobsen, 2000; Lelièvre et al., 2012) or use approaches that invert directly for reservoir and rock properties (e.g. Hoversten et al., 2006; Dell'Aversana et al., 2011). An alternative way of considering structural information is to use sharp-boundaries in joint inversions (e.g. Juhojuntti and Kamm, 2015) that allow strong contrasts at interfaces, but inherently assume that the subsurface consists of a number of distinct layers, an assumption that is not necessarily true. Finally, several authors couple data by clustering (e.g. Paasche and Tronicke, 2007; Lelièvre et al., 2012; Sun and Li, 2013) that can be considered more appropriate than simplified petrophysical assumptions for some geological conditions.

The objective of this paper is the introduction and test of a new joint inversion strategy, in which we try to mitigate the four problems raised above. Our scheme *JINV2D* is a cell-based non-linear 2-D joint inversion that combines magnetotelluric (MT), seismic P-wave tomography and gravity data by using petrophysical information and has been mainly developed to investigate sub-basalt structures that are often not well-resolved by reflection seismic data. To avoid relative scaling (1st problem) we use a cooperative joint inversion in which the inversion steps are performed separately for each method and the otherwise independent inversions are linked by employing constraints that account for parameter relationships. Core element of our proposed joint inversion is an automated adaptive coupling scheme, which

allows for flexible inclusion of these constraints. This adaptive scheme ensures a robust convergence (2nd problem) for all methods and allows the obtained physical parameter models to deviate from the initial assumed parameter relationships, which makes this assumption less rigid (4th problem). Different resolutions of the various methods (3rd problem) are handled by making the behavior of the coupling constrains dependent on the relative resolution power of the methods. Finally, we include a method that allows the exchange of structural information between the parameter models in addition to petrophysical information.

Within the methodology section we first outline our joint inversion strategy. We then focus on a more detailed description of its implementation. The adaptive joint inversion scheme is tested on a synthetic model that is associated with settings that are typical for sub-basalt problems. Finally, we present joint inversion results from a real data example for sub basalt imaging from the Faroe-Shetland Basin, where wide angle streamer seismic, marine MT and marine gravity data are combined.

2. METHODOLOGY - OUTLINE OF JOINT INVERSION STRATEGY

2.0.1. Parametrization

The 2-D grids used for the forward modeling routines are composed of rectangles to which constant velocity, density and resistivities are assigned. Cell sizes are adapted individually for each method to account for numerical accuracy issues and computational efficiency. For the inversion we use a coarser grid created by combining several forward modelling cells, since the

presented inversions (independent on the methods) do not resolve the model at the numerical precision required for the forward problem. We choose the same inversion grid for all three methods such that different physical parameters can be easily linked to each other in the joint inversion and the method with highest resolution defines the cell sizes to avoid data mismatches associated with improper discretization.

2.0.2. Forward modeling

Because standard forward modelling techniques are implemented for all methods we only briefly summarize the routines and refer to the literature for further information. For seismic tomography first-arrival times are computed by an eikonal solver (Podvin and Lecomte, 1991) and afterwards the associated ray-paths are constructed by a steepest descent method (Aldridge and Oldenburg, 1993). For gravity modelling the z-component of the attractions from all cells are calculated for each gravity station and the resulting gravity responses are then obtained by summing the contributions from all cells (Bear et al., 1995). Border effects for the gravity due to the finite extent of the 2-D model are avoided by adding semi-infinite horizontal rods at the left and right boundary. For MT we use a 2-D frequency-domain finite-element code to calculate both the transverse electric (TE) and transverse magnetic (TM) mode impedances for a number of frequencies (Wannamaker et al., 1987).

2.0.3. Inversion procedure

A Hessian-free Gauss-Newton minimization method (Nocedal and Wright, 2006), which has a rapid quadratic convergence as long as the local behavior

is not strongly non-linear, is used to iteratively solve the linearized inversion problems. To solve the associated linear system, the LSQR solver from Paige and Saunders (1982) is employed. We use first-arrival times of all shot-receiver combinations as seismic data ($\mathbf{d}^{seis.}$), the z-component of the gravity field at all measuring locations as gravity data ($\mathbf{d}^{grav.}$) and real and imaginary part of the impedances for a number of frequencies and at all MT stations as MT data ($\mathbf{d}^{MT}$). Model parameters are seismic velocities $\mathbf{m}^{vel.}$, densities $\mathbf{m}^{dens.}$ and logarithmic values of resistivities $\mathbf{m}^{res.}$ of the inversion cells. Smoothing constraints based on Laplacian differences (Ammon and Vidale, 1993) are employed as regularization to stabilize the inversion. The inversion step lengths are adjusted at every iteration through a line search procedure (Moré and Thuente, 1994).

Unlike most other joint inversion schemes, the inversion processes of the individual methods are performed separately from each other. The required coupling between the individual inversions is provided by an additional constraint in the objective function for each inversion accounting for relationships between the three model parameters $\mathbf{m}^{res.}$, $\mathbf{m}^{vel.}$ and $\mathbf{m}^{dens.}$. We choose this approach since it avoids the necessity to find an adequate scaling between terms related to different methods in a combined objective function (i.e. Moorkamp et al., 2011). However, synchronization between the individual processes is required to treat all methods equally. This is achieved by performing a single inversion step for all three methods and updating the associated coupling constraints before the next iteration is started.

For our joint inversion method the objective functions for the MT, seismic

and gravity inversion Φ^{MT}, $\Phi^{seis.}$ and $\Phi^{grav.}$ are:

$$\begin{aligned}
\Phi^{MT} &= \Phi^{MT}_{(d)}(\mathbf{m}^{res.}) + (\lambda^{MT})^2\Phi^{MT}_{(m)}(\mathbf{m}^{res.}) + (\mu^{MT})^2\Phi^{MT}_{(c)}(\mathbf{m}^{res.}, \tilde{\mathbf{m}}^{res.}) \longrightarrow min \\
\Phi^{seis.} &= \Phi^{seis.}_{(d)}(\mathbf{m}^{vel.}) + (\lambda^{seis.})^2\Phi^{seis.}_{(m)}(\mathbf{m}^{vel.}) + (\mu^{seis.})^2\Phi^{seis.}_{(c)}(\mathbf{m}^{vel.}, \tilde{\mathbf{m}}^{vel.}) \longrightarrow min \\
\Phi^{grav.} &= \Phi^{grav.}_{(d)}(\mathbf{m}^{dens.}) + (\lambda^{grav.})^2\Phi^{grav.}_{(m)}(\mathbf{m}^{dens.}) + (\mu^{grav.})^2\Phi^{grav.}_{(c)}(\mathbf{m}^{dens.}, \tilde{\mathbf{m}}^{dens.}) \longrightarrow min
\end{aligned}$$

where $\Phi_{(d)} = [\mathbf{g}(\mathbf{m}) - \mathbf{d}_{obs.}]^T\mathbf{D}^T\mathbf{D}[\mathbf{g}(\mathbf{m}) - \mathbf{d}_{obs.}]$ are the data terms, $\Phi_{(m)} = \mathbf{m}^T\mathbf{C}^T\mathbf{C}\mathbf{m}$ are the regularization terms, $\Phi_{(c)}$ are the terms that account for the parameter relationships, $\mathbf{d}_{obs.}$ is the vector containing the observed data, $\mathbf{g}(\mathbf{m})$ is the vector containing the calculated data obtained by forward modeling, $\mathbf{D}^T\mathbf{D} = \mathbf{C}^{-1}_{(d)}$ is the inverse of the data covariance matrix and $\mathbf{C}$ is the roughness matrix (containing discrete first-order derivatives). The impact of the individual terms is governed by the regularization and coupling parameters λ^{MT}, $\lambda^{seis.}$, $\lambda^{grav.}$ and μ^{MT}, $\mu^{seis.}$, $\mu^{grav.}$, respectively.

While the data terms $\Phi_{(d)}$ and regularization terms $\Phi_{(m)}$ are commonly used in all types of inversions, the coupling terms $\Phi_{(c)}$ are particular to joint inversion. $\Phi_{(c)}$ express the coupling between the individual inversions as minimization problems ($\Phi_{(c)} \longrightarrow min$) and describe, in our case, how far the model parameters $\mathbf{m}^{res.}$,$\mathbf{m}^{vel.}$ and $\mathbf{m}^{dens.}$ deviate from the proposed rock parameter relationships. To determine the constraints of the $\Phi_{(c)}$ for all N inversion cells, projections $\tilde{\mathbf{m}}$ onto the pre-defined relationship curve are calculated from the physical parameters $\mathbf{m}$. The distances between the model parameters $\mathbf{m}$ and their projections $\tilde{\mathbf{m}}$ are then used to define the minimiza-

tion problems for $\Phi_{(c)}$ as:

$$\begin{aligned}
\Phi_{(c)}^{MT.}(\mathbf{m}^{res.}, \tilde{\mathbf{m}}^{res.}(\mathbf{m}^{res.}, \mathbf{m}^{vel.}, \mathbf{m}^{dens.})) &= \sum_{j=1}^{N} (m_j^{res.} - \tilde{m}_j^{res.}(m^{res.}, m^{vel.}, m^{dens.}))^2 \\
\Phi_{(c)}^{seis.}(\mathbf{m}^{vel.}, \tilde{\mathbf{m}}^{vel.}(\mathbf{m}^{res.}, \mathbf{m}^{vel.}, \mathbf{m}^{dens.})) &= \sum_{j=1}^{N} (m_j^{vel.} - \tilde{m}_j^{vel.}(m^{res.}, m^{vel.}, m^{dens.}))^2 \\
\Phi_{(c)}^{grav.}(\mathbf{m}^{dens.}, \tilde{\mathbf{m}}^{dens.}(\mathbf{m}^{res.}, \mathbf{m}^{vel.}, \mathbf{m}^{dens.})) &= \sum_{j=1}^{N} (m_j^{dens.} - \tilde{m}_j^{dens.}(m^{res.}, m^{vel.}, m^{dens.}))^2
\end{aligned}$$

(Note that the all three $\Phi_{(c)}$ terms are dependent on all three physical parameters.)

Practical meaning of this implementation is that associated constraints pull the model parameters $\mathbf{m}^{res.}$, $\mathbf{m}^{vel.}$ and $\mathbf{m}^{dens.}$ towards the relationship curves such that the relative behaviour of the different physical models is approximately described by the parameter relationships.

The projection method proposed here (see Appendix A for a detailed description) has the advantage that the impact of all physical parameters is equally balanced independent of their parameter ranges. However, it is only applicable for parameter relationships that have a strictly monotonic behaviour.

2.0.4. Adjust the projection by using model resolution estimates

Another advantage of the way the projection is implemented is the possibility to take into account the resolving power of different methods at each individual cell. In the Appendix B we describe how the projection presented in Appendix A is modified such that it has the following behaviour: if method 1 (e.g. seismic) has a high resolution and the other methods (e.g. MT and gravity) have low resolutions in an inversion cell, the resulting parameters

from the projection are very similar to the one obtained from the method 1 e.g. velocity of the projection is very similar to the velocity of the seismic model and resistivity (density) of the projection are very similar to the resistivity (density) calculated from the seismic velocity model by means of the parameter relationships (see also black dot in Fig. A.18b in Appendix A). If the resolution powers of the different methods are in a similar range, the parameters from the projections are averages which are similarly affected by all model parameters. Such implementation improves the performance of the joint inversion and reduces the number of required iterations to reach an adequate data misfit, because the projection direction is guided spatially flexible by the relative impact of the different data sets.

A good measure for evaluating the resolution of a method is the diagonal of the model resolution matrix $\mathbf{R} = ((\mathbf{G}^T\mathbf{G} + \lambda^2\mathbf{C}^T\mathbf{C})^{-1}\mathbf{G}^T)\mathbf{G}$ (where $\mathbf{G} = \mathbf{DS}$ and $\mathbf{S}$ is the sensitivity matrix). $\mathbf{R}$ is normalized to 1.0 and 0.0, where 1.0 indicates perfectly and 0.0 not resolved at all parameters, respectively. Retrieving the diagonal by calculating the complete resolution matrix, however, is difficult for large inverse problems since it requires computer memory of the size $N \times N$. We therefore use instead an efficient stochastic estimation of the resolution matrix diagonal suggested by MacCarthy et al. (2011). They arrange the equation for the model resolution matrix such that its diagonal can be solved with the same linear system as used for the corresponding linearized inversion problem (see equations 7 to 9 in their publication). (As in their equation 9 we consider the regularization terms in the calculation of the resolution matrix diagonal; however, we ignore the coupling terms.) Their approach is based on the work from Bekas et al.

(2007), who developed a statistical procedure to determine the diagonal of a large $P \times P$ matrix by iteratively applying a sequence of P-length random vectors to this matrix. Although the quality of the diagonal estimates depends onto the number of iterations, we restrict them to maximum 5000 in our runs to keep computation times low. If the diagonal elements are assigned to the associated inversion cells, the obtained models showing the resolution estimates appears slightly noisy. To remove this noise and smooth the resolutions estimates in the spatial directions, the median of resolution parameters is determined from all neighbouring cells for each cell and applied as the final resolution measures in the parameter projection.

2.0.5. Adaptive determination of the coupling parameters

In our experience it is necessary need to keep the coupling parameters μ flexible during the inversion process. This can be explained as follows. Each method has its natural convergence path through the model space to decrease its data misfit. These paths may differ substantially for the different methods (e.g. MT and seismic tomography are strongly non-linear methods, whereas gravity is a linear method). Since the projection on the parameter relationship curve depends on the model parameters of all three methods, it is possible that, during the inversion process, the natural convergence direction for some of the methods points in a completely different direction in the model space to that the associated coupling constraint points. This can even occur when the parameter relationships perfectly describe the rock property behaviour. If the weight of the coupling parameter μ is chosen too high, the associated constraints force the parameter models in wrong directions, the convergence of the inversion is slowed down and the individual inversion

may then get trapped in local minima where the data misfit is not properly minimized. In contrast, coupling strengths which are too weak may lead to parameter models which are barely linked and, hence, the potential of increasing the resolution through joint inversion is then not utilized.

To avoid such scenarios we implement a scheme to vary the coupling parameters μ^{MT}, $\mu^{seis.}$ and $\mu^{grav.}$ for the individual methods adaptively and independently from each other during the inversion process. The adaption of the coupling parameters is implemented in exactly the same way for all three methods and we thus explain the procedure here for one method only.

The adaptation criterion is based on the idea that the coupling constraint should affect the convergence behaviour of the objective function at each iteration, k, by the same amount. It states that the incremental change of the sum of the data and regularization terms of the objective function

$$\Delta\Phi_{(d+m)}^{Constr.,k} := (\Phi_{(d)}^{Constr.,k} + \lambda^2\Phi_{(m)}^{Constr.,k}) - (\Phi_{(d)}^{Constr.,k-1} + \lambda^2\Phi_{(m)}^{Constr.,k-1}) \quad (1)$$

for our constrained inversion should correspond to a specified portion D (with $1.0 > D > 0.0$) of the same terms

$$\Delta\Phi_{(d+m)}^{Ref.,k} := (\Phi_{(d)}^{Ref.,k} + \lambda^2\Phi_{(m)}^{Ref.,k}) - (\Phi_{(d)}^{Constr.,k-1} + \lambda^2\Phi_{(m)}^{Constr.,k-1}) \quad (2)$$

for a reference inversion without constraint ($\mu_k = 0$):

$$\Delta\Phi_{(d+m)}^{Constr.,k} = D\Delta\Phi_{(d+m)}^{Ref.,k} \quad (3)$$

The meaning of the criterion is illustrated in Figure 1.

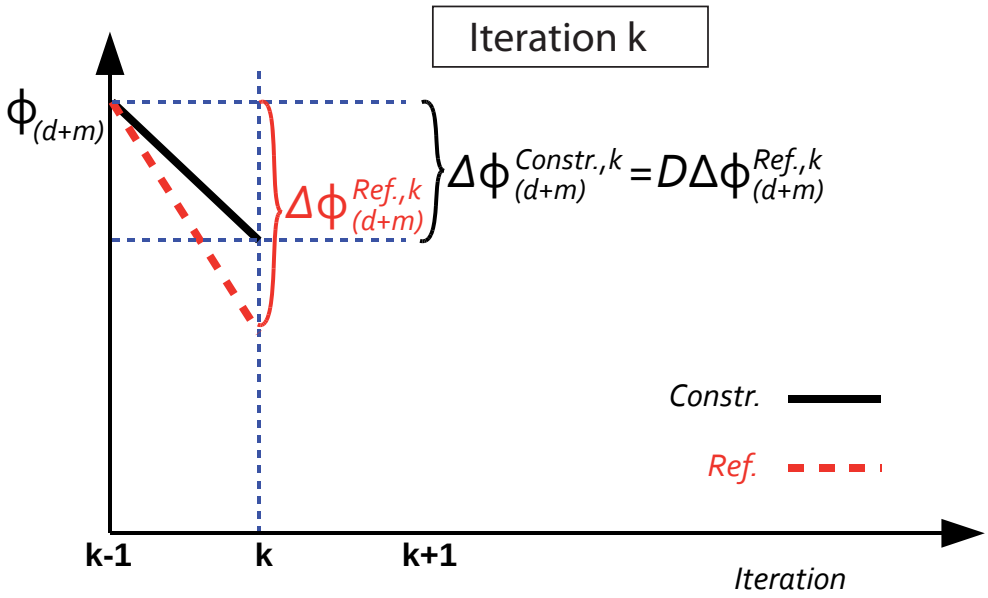

Figure 1: Sketch illustrating the adaption criterion for the coupling parameters at iteration. The parameter μ is chosen such that the change of data term plus regularization term of the objective function $\Delta\Phi^{Constr.,k}_{(d+m)}$ of the constrained inversion at iteration k (black line) is a predetermined factor D smaller than for the change of these terms $\Delta\Phi^{Ref.,k}_{(d+m)}$ for the unconstrained inversion (red line).

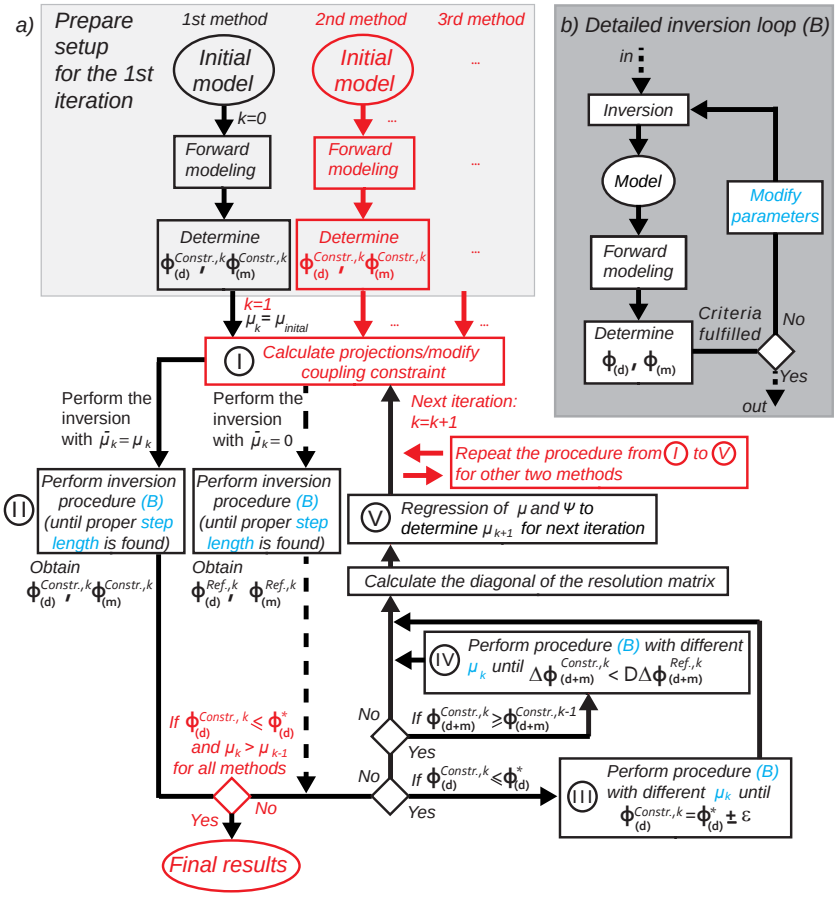

Figure 2: a) Flowchart illustrating the adaptive inversion scheme. The scheme shows the procedure for only one of the methods. For the other methods the procedure is equivalent. Steps where information from the other methods are involved are highlighted in red colors. Roman numerals mark the different steps that are explained in the body of the text. The grey box b) shows an inversion loop, which is performed at different stages of the procedure (see blue letters (B) in a)) and in which the fulfillment of different criteria are tested: At stage II the step length is varied until the Wolfe conditions (Nocedal and Wright, 2006) are satisfied and at stages III and IV μ_k is varied until criteria are reached that consider the behavior of the objective functions.

Although this criterion specifies how the terms $\Delta\Phi_{(d+m)}^{Constr.}$ of our constrained inversion should change at each iteration step, it does not explicitly depend on μ. This means that an additional assumption linking the variations of $\Delta\Phi_{(d+m)}$ with the ones of the μ values is required to be able to develop an adaptive scheme. Here, we assume that μ is approximately linear with the normalized incremental change of the objective function Ψ_l for a number of L successive iterations:

$$\mu_l \approx p_k^{(0)} + p_k^{(1)} \underbrace{\frac{\Delta\Phi_{(d+m)}^{Ref.,l} - \Delta\Phi_{(d+m)}^{Constr.,l}}{\Delta\Phi_{(d+m)}^{Ref.,l}}}_{=:\Psi_l} \qquad \text{with} \quad l = k-(L-1), ..., k \tag{4}$$

To update μ at every iteration the criterion and the assumption (eq. 4) are combined in the scheme shown in Figure 2.

For iteration k:

1. the coupling constraint associated with the parameter relationship is determined (see Ⓘ in Fig. 2)
2. two model updates (inversion steps) - one with and one without the coupling constraint - are performed (see Ⓘ‌Ⓘ and panel (B) in Fig. 2).
3. forward calculations are conducted for both updated models and the associated terms of the objective functions $\Phi_{(d+m)}^{Constr.,k}$ and $\Phi_{(d+m)}^{Ref.,k}$ are determined. Steps 2 and 3 are repeated with different inversion step lengths as long as the step length criteria (Moré and Thuente, 1994) are not satisfied (see Ⓘ‌Ⓘ and box (B) in Fig. 2).
4. the diagonal of the resolution matrix is calculated to adjust the projection.

5. a linear regression of normalized incremental change of the objective functions $\Psi_{\tilde{l}}$ and coupling parameters $\mu_{\tilde{l}}$ from a number of previous iterations $\tilde{l} = k - (\tilde{L} - 1), ..., k$ is carried out (see ⓥ in Fig. 2). The axis intercept $p_k^{(0)}$ and slope $p_k^{(1)}$ from the linear regression are then used to calculate the coupling parameter μ_{k+1} for the next iteration by means of the formula

$$\mu_{k+1} = (1 - D)p_k^{(1)} + p_k^{(0)} \quad , \tag{5}$$

which is obtained by a combination of eq. 3 and eq. 4.

6. Steps 1) to 5) are repeated for the other two methods.

Steps 1) to 6) are repeated at each iteration.

The convergence speed is controlled by the parameter D and the number of previous iterations $\tilde{L}$, from which information is used in the regression. For larger values of D it is assumed that the data misfit for the corresponding method decreases generally faster during the inversion process (see eq. 3) and that the resulting μ are smaller (see eq. 5). This means that the associated method is less coupled. For larger values of $\tilde{L}$ the adaptive algorithm reacts more inertly if the effect of the relationship constraint onto the convergence behaviour changes. On the other hand, regression becomes less sensitive to outliers and, hence, the algorithm can be considered as more robust.

Regression results and consequently updates of μ only depend on the distribution of $\mu_{\tilde{l}}$ and $\Phi_{\tilde{l}}$ from a small number of previous iterations (typically < 6), therefore updated μ's are only local and not global estimates of the best suited values for the coupling at the corresponding iteration. However, we tested our scheme on different synthetic examples and observe that the

implemented adjustment of coupling parameters is in most cases sufficient to obtain stable convergence behaviour for individual inversions. The same tests lead us to conclude that D should be in the range of 0.4 - 0.9 and $\tilde{L}$ should be in the range of 2 - 5 to ensure robust and fast convergence.

Nonetheless, under some circumstances the assumption of eq. 4 may not be appropriate for a specific method and iteration and the determined update of μ results in an increase of the remaining objective function $\Phi_{(d+m)}^{Constr.,k} \geq \Phi_{(d+m)}^{Constr.,k-1}$. To guarantee convergence, the value of μ_k is then recalculated in such cases: The inversion loop is repeated for different μ-values (see box (B) and ⓘⓥ in Fig. 2) and by means of interpolation (bisection method) an appropriate coupling parameter is found which satisfies the condition $\Delta\Phi_{(d+m)}^{Constr.,k} < D\Delta\Phi_{(d+m)}^{Ref.,k}$. We emphasize that the procedure to recalculate μ is often significantly more time-consuming than determining μ by adaption, because more forward calculations are required (typically a factor 2-4). Even if μ values determined from the adaptive procedure provide model updates that only roughly satisfy the criterion, it is more useful to take information from previous iterations to avoid slowing down the joint inversion process.

When the data term of the objective function gets smaller than the specified target misfit $\Phi_{(d)}^{Constr.} \leq \Phi_{(d)}^{\star}$ (typically associated with an error weighted data misfit close to 1.0), in principal a solution is found for the associated method. Modification of the associated μ by the adaptive algorithm is then no longer required and one option would be to keep μ unchanged in the following iterations. However, since we are interested in finding the solution with the strongest possible coupling, we want to identify instead the largest μ that is compatible with the data. For this purpose, we choose a similar

procedure as proposed by Constable et al. (1987) and de Groot-Hedlin and Constable (1990), who searches for the smoothest model that explains the data (Occam's inversion). However, in contrast to their approach we consider μ^{-1} (and not λ^{-1}) as the Lagrangian multiplier that is adjusted when $\Phi^{\star}_{(d)}$ is reached for the associated method. The inversion loop is therefore repeated for a number of different μ and an interpolation method is employed (bisection method) to find the coupling parameter with the largest value which satisfies $\Phi^{\star}_{(d)} - \epsilon \leq \Phi^{Constr.}_{(d)} \leq \Phi^{\star}_{(d)} + \epsilon$ (with ϵ being a small positive quantity) for the next iteration (see box (B) and ⓘⓘⓘ in Fig. 2).

The complete inversion procedure stops, when all methods reach their specified target misfits and no increase in the coupling parameters can be achieved in the next iteration.

2.0.6. Adjustment of smoothing parameter

We have tested different methods to adjust the smoothing during the inversion process (including the adaptive scheme used to modify μ). They show that the convergence behavior is less influenced by the regularisation than by the coupling parameters. Several of the conventional techniques to modify λ demonstrate that they are well suited to reach the target misfits and we use a simple technique with a cooling-schedule-type behaviour proposed by Lelièvre et al. (2012). An initially large value for λ is chosen that is reduced with increasing number of iterations. In this way progressively more detailed structures are introduced into the models. The factor of reduction $1/\nu_k$ from one iteration to the next:

$$\frac{1}{\nu_k} = \frac{\lambda_{k+1}}{\lambda_k} \tag{6}$$

is determined by

$$\begin{aligned} \nu_k &= 1 + \tau \mid \Phi^k_{(d)}/\Phi^\star_{(d)} - 1 \mid \qquad \text{if} \quad \Phi^k_{(d)} > \Phi^\star_{(d)} \\ \nu_k &= 1 \qquad\qquad\qquad\qquad\qquad\quad \text{if} \quad \Phi^k_{(d)} \leq \Phi^\star_{(d)}. \end{aligned}$$

Typical values used for the parameter τ are in the range of 0.02 - 0.2. The rate of reduction depends on the actual target misfit $\Phi^\star_{(d)}$ and ν_k remains constant if the target misfit is reached. To avoid overly fast reduction of the regularization, ν is limited to values between 1 and 2. If a regularization parameter becomes smaller than a specific threshold value $\lambda^\star$, the procedure stops and the regularization remains unchanged ($\lambda = \lambda^\star$) for further iterations to avoid instabilities in the inversions. Values for $\lambda^\star$ used in this study range from 0.7 to 1.0 depending on the methods.

2.0.7. Implementation of structural cross-coupling

The adaptive method can be extended to include structural information at the same time. We have implemented an approach suggested by Günther and Rücker (2006), where cross-coupling is achieved through mutually controlling smoothing constraints of a given parameter model by the roughness distribution from other parameter models. Thus a strong spatial parameter contrast existing in at least one of the parameter models can be transferred to the other parameter models.

This cross-coupling scheme is implemented as follows. Firstly, at the k-th iteration the roughness vectors $\mathbf{r}$ are calculated for all models using:

$$\begin{aligned} \mathbf{r}^{res.} &= \mathbf{C}\mathbf{m}^{res.} \\ \mathbf{r}^{vel.} &= \mathbf{C}\mathbf{m}^{vel.} \\ \mathbf{r}^{dens.} &= \mathbf{C}\mathbf{m}^{dens.} \end{aligned}$$

where $\mathbf{C} \in \mathbb{R}^{B \times N}$ is the roughness matrix (where B is the number of cell boundaries and N the number of inversion cells). Secondly, weights $w_1, ..., w_B$ are determined for each method by means of the associated roughness vectors:

$$\begin{aligned} w_j &= min(h_j, 1.0) \quad \text{with} \quad h_j = \left(\frac{\alpha}{\frac{|r_j|}{\|\mathbf{r}\|} + \alpha} \right)^{\beta} \\ &\text{where the constants } \alpha \text{ and } \beta \text{ have typical values of 0.1 and 1.0.} \end{aligned} \tag{7}$$

Finally, the weights for the model of one method are used to modify the regularisation terms for the other models:

$$\begin{aligned} \Phi_{(m)}^{MT} &= \left\| \sqrt{\mathbf{W}^{vel.}\mathbf{W}^{dens.}}\mathbf{C}\mathbf{m}^{res.} \right\|_2^2 \\ \Phi_{(m)}^{seis.} &= \left\| \sqrt{\mathbf{W}^{res.}\mathbf{W}^{dens.}}\mathbf{C}\mathbf{m}^{vel.} \right\|_2^2 \\ \Phi_{(m)}^{grav.} &= \left\| \sqrt{\mathbf{W}^{res.}\mathbf{W}^{vel.}}\mathbf{C}\mathbf{m}^{dens.} \right\|_2^2 \end{aligned}$$

$$\text{with} \qquad \mathbf{W} = diag\,(w_1, ..., w_B) \qquad \text{(weighting matrix)}$$

The procedure of this structural cross-coupling strategy is illustrated for one iteration and two methods in Figure 3. In our inversion scheme the structural-cross coupling is performed immediately at the beginning of each iteration (before the coupling constraints for the petrophysical relationships are calculated; see ① in flowchart in Fig. 2).

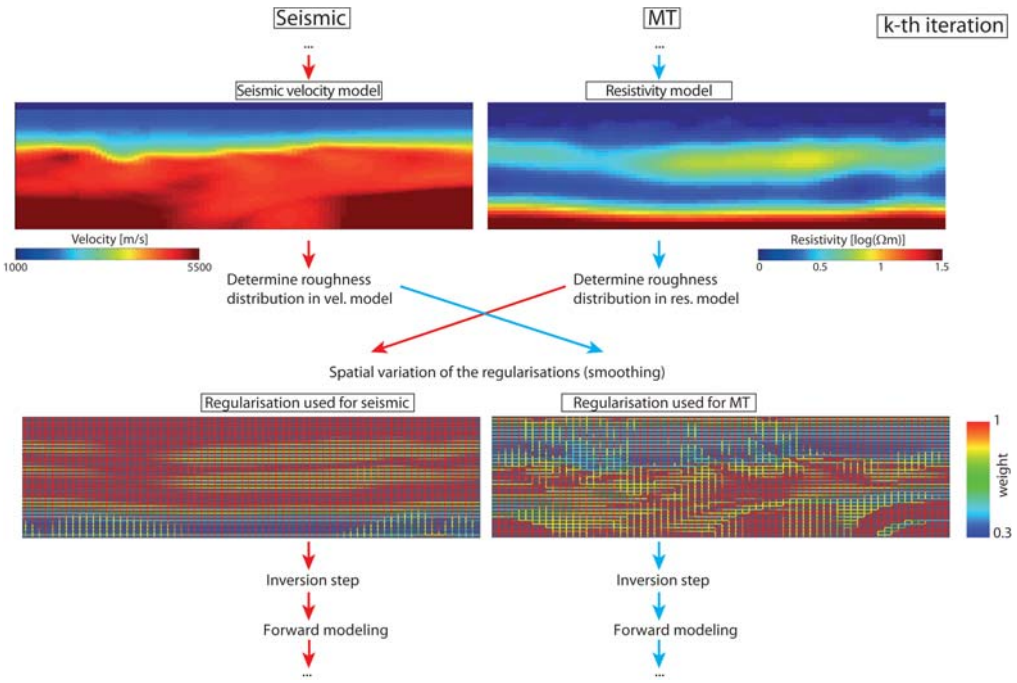

Figure 3: Sketch illustrating the structural cross-coupling strategy proposed by Günther and Rücker (2006). In the upper panel we show a velocity and resistivity model derived at the k-th iteration for the inversion of seismic tomography and MT data for a synthetic sub-basalt model (see next section for a more detailed discussion). The roughnesses of one model is used to calculate the weights for the smoothing constraints of the other model (see bottom panels); and vice versa.

3. SYNTHETIC TEST ON A SUB-BASALT MODEL

We test our adaptive inversion scheme on a 2-D synthetic basalt model. The model was proposed by Martini et al. (2005) to simulate realistic seismic and non-seismic data and to develop strategies for geophysical data integration for sub-basalt problems. It is known that imaging of sub-basalt sediments with reflection seismic techniques is complicated due to absorption, scattering and transmission effects and the presence of peg-leg multiples (e.g. Purnell, 1992). Although many of the difficulties facing conventional seismic profiles can be overcome by recording long offset data (e.g. Fliedner and White, 2003), resolution of sub-basalt structures in seismic sections is still largely limited. Therefore multi-parametric approaches (Hautot et al., 2007; Panzner et al., 2014; Hoversten et al., 2015) and joint inversion strategies (Heincke et al., 2006; Colombo et al., 2008; Manglik et al., 2009; Jegen et al., 2009) have been developed to gain additional information from sub-basalt structures. Our simplified model contains two mostly horizontal layers that have high velocity, resistivity and density (Fig. 4, upper panels). The upper layer is associated with a sequence of basalt flows and the lower layer is considered to be basement. Above the basalt and between the basalt and the basement there are layers with lower physical property values, which represent sediments over and under the basalt layer, respectively. Everywhere in the synthetic model the three physical parameters resistivities ρ (in Ωm), velocities v_p (in m/s) and densities d (in g/cm^3) are linked by the density-velocity and resistivity-velocity relationships

$$d = 0.0002\ v_p + 1.7 \tag{8a}$$

and

$$\log_{10}(\rho) = 1.20\ log_{10}(v_p) - 3.86 \qquad \text{for } v_p < 3600$$
$$\log_{10}(\rho) = 6.46\ log_{10}(v_p) - 22.57 \qquad \text{for } v_p > 3600 \tag{8b}$$

that are derived from commercial and ODP borehole data collected on the north west European margin (Jegen et al., 2009). At the top of the model a 400 m thick layer is added representing seawater. Physical properties of the water layer remain unchanged during the inversion ($\rho = 0.3$ Ωm, $v_p = 1560$ m/s, $d = 1.0$ g/cm^3). The model is discretized for inversion into 85×71 cells with sizes of 400×100 m in the horizontal and vertical directions, respectively.

The seismic and gravity data sets for the synthetic tests are generated using the same forward modeling routines as in the joint inversion. However, to reduce the impact of modelling effects that are associated with using the same forward codes, discretisations of the model for data generation are significantly finer than the ones used in the forward modeling routines during inversion. For MT we employ a different modelling program (2-D MT code from Tarits, 1984) to calculate the impedance estimates from the synthetic model to the one (2-D MT code from Wannamaker et al., 1987) we use in the joint inversion.

For seismics we consider an OBS data set with 6018 first arrivals from 177 shot and 34 receiver positions, respectively. Both shot positions at the surface and receivers at the seafloor are equally spaced ($\Delta x_{\text{shots}} = 200$ m and $\Delta x_{\text{receivers}} = 1000$ m). The gravity data set is composed of 60 stations

453 located on the sea surface ($\Delta x_{\text{grav. station}} = 500$ m). The MT data set consists
454 of 33 stations that are equally spaced along the seafloor ($\Delta x_{\text{MT station}} = 1000$
455 m). Such short station intervals are still uncommon for MT field surveys.
456 However, the objective of this exercise is to evaluate the general performance
457 of our joint inversion scheme and at this stage we prefer to use models, where
458 the individual methods show a dense and uniform coverage. We use as input
459 for the inversions both TE and TM mode data with 15 frequencies over a
460 range of $2.5 \cdot 10^{-5}$ to 1 Hz. Gaussian noise is added to all data sets with
461 standard deviations $\sigma_{seis.} = 10$ ms, $\sigma_{grav.} = 0.05$ mgal and $\sigma_{MT} = 2\%$ of the
462 abs. values, respectively.

463 To obtain a qualitative understanding about the resolution power of the
464 individual methods we plot estimates of the diagonal elements of the reso-
465 lution matrix (Fig. 4, lower panels) for the synthetic model. Based on this
466 measure, seismic rays from first arrivals only provide information about the
467 top of basalt and the overlying sediments. Resolution of gravity data varies
468 smoothly and decreases with depth, as is typical for potential field methods.
469 MT is sensitive to the conductive sediments, but not to the highly resistive
470 basalt layer and basement. At the left and right border high resolution values
471 in the (gravity and) MT are related to a background layer model required
472 for both methods (gravity: semi-infinite horizontal sheets; MT: cells at the
473 border, whose size increasing with the distance from the model boundary).
474 The resolution estimate shows that all three methods are sensitive to differ-
475 ent subsets of structural elements of the model and thus contain common but
476 also complementary information about the entire structure. It is the com-
477 plementary information content in the data sets which allows the derivation

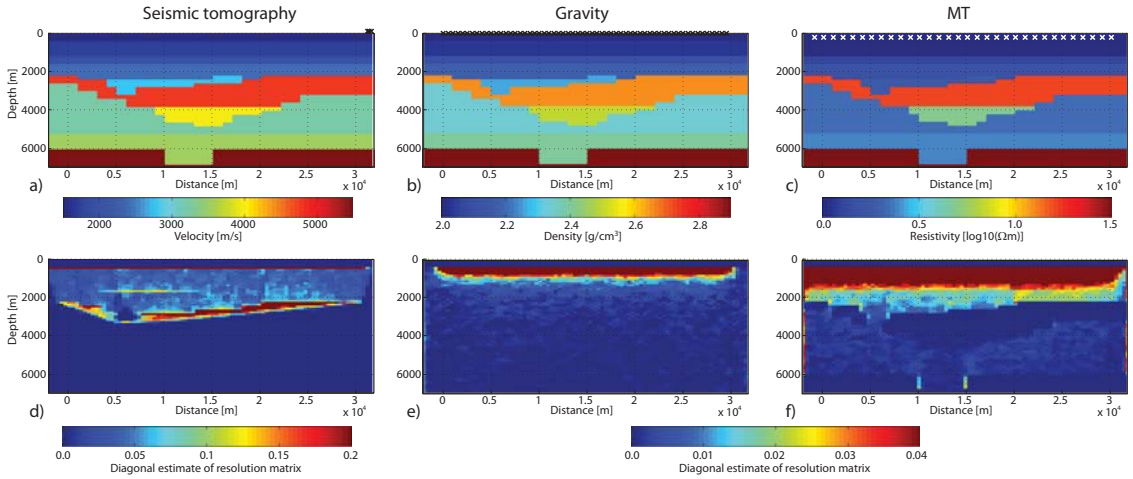

Figure 4: Upper panels: a) Velocities, b) densities and c) resistivity distributions representing the synthetic sub-basalt model. Circles denote locations of OBS stations and crosses highlight positions of shots in a), gravity stations in b) and MT stations in c). Lower panels: Approximations of the diagonal elements of the resolution matrices for each method (see section 2.0.4 for further details about their calculation). High values of resolution are found at the very right and left border of the gravity and MT data (see panels e,f) due to necessity to include a background gravity and MT model.

of an improved model through a joint inversion process.

3.1. Results from the individual inversions

Before presenting the results of the joint inversion we show results of inverting each of the datasets separately. For seismic inversion we use a starting model that consists of horizontal velocity layers, but for gravity and MT inversions starting models are homogenous half-space models. Cell sizes are the same as in the joint inversion. In contrast to the joint inversions, a conventional Occam's type inversion is performed for the individual inversions;

i.e. if the target misfit is reached in the inversion procedure, λ is adjusted to find the smoothest model that explains the data.

Results of these individual inversions (Fig. 5, Row 1) show that none of the three methods is able to resolve the basalt layer, the underlying sediments and the basement at the same time, which confirms our prediction based on the resolution analysis. Refraction seismic tomography only resolves the velocity distribution down to the top of basalt. The gravity inversion does not resolve any structure. The MT inversion identifies high and low resistive structures that can be associated with the basement and conductive sediments, respectively, however the resistive basalt layer is not well resolved (too low resistivities and inaccurate shape).

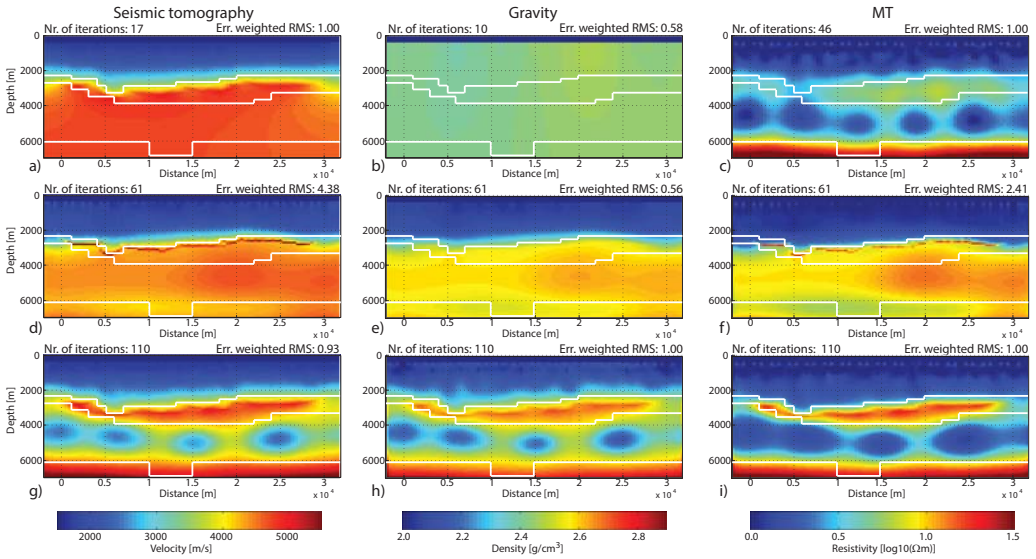

Figure 5: First row: Final results from individual Occam seismic, gravity and MT inversions. Second row: Final results from a petrophysical joint inversion, in which the strengths of coupling is kept constant ($\mu^{MT} = \mu^{seis.} = \mu^{grav.} = 0.25$) during the inversion process. Third row: Final results from a petrophysical joint inversion, in which the coupling constraints are adapted at each inversion step (rate of adaption $D^{MT} = D^{seis.} = D^{grav.}$ is 0.7 and 3 previous iterations $\tilde{L}$ are considered in the regression). Unlike in the tests presented in Fig. 6 the projection is not modified by a resolution measure. Locations of the basalt layer and the basement are outlined with white lines.

3.2. Starting models for the joint inversions

To determine the starting models for the joint inversions, first, individual seismic tomography inversion is performed. We then use the parameter relationship (eq. 8a) to transfer the initial velocity model to a density model. For this model an individual gravity inversion is performed. During this gravity inversion, density values of cells covered by seismic rays are kept fixed. Model densities from the inversion results are finally transferred back to velocities and also resistivities (eqs. 8a and 8b). This procedure determines starting models that are already relatively close the actual subsurface; a strategy commonly used in joint inversion applications. We demonstrate later in this section that we obtain similarly good final joint inversion results by using starting models that are not linked to each other and are further away from the true model.

3.3. Results from petrophysically linked joint inversions

First, we test our joint inversion scheme with coupling parameters that remain constant during the inversion process ($\mu^{seis.} = \mu^{grav.} = \mu^{MT} = 0.25$). All methods are equally weighted for projections onto the parameter relationships, which means the resolution of each of the methods is not taken into account. We also do not include structural cross coupling, however, we gradually reduce the smoothing parameters (from starting values of $\lambda^{seis.} = \lambda^{grav.} = \lambda^{MT} = 0.25$) as described in the section 2.0.6. The final results for this test are not satisfying (Fig. 5, Row 2); the shape of high velocity, resistivity and density anomalies does not coincide with the shape of the basalt in our synthetic model and there are no low velocity, resistivity nor density anomalies can be associated with sub-basalt sediments. Error weighted data

misfits $d_{RMS} = \sqrt{\frac{1}{M}\sum_{i=0}^{M}(\frac{g(\mathbf{m})_i - d_i}{\sigma_i})^2}$ do not reach the target misfit of 1.0 for seismic ($d_{RMS}^{seis.} = 4.38$) and MT ($d_{RMS}^{MT} = 2.41$), respectively. It is likely that the inversion processes get trapped in local minima relatively close to the actual starting models. (In contrast, the error weighted data misfit for the gravity $d_{RMS}^{grav.} = 0.56$ remains clearly smaller than the target misfit of 1.0, although λ is increased, when the target misfit is reached (Occam's inversion). This indicates that the amount of smoothing has little impact onto the data misfit of the gravity.)

In the next step the joint inversion is repeated using the same starting model and initial coupling values, however, now we adaptively modify our coupling parameters. D is set to relatively high values of $D^{seis.} = D^{grav.} = D^{MT} = 0.7$ to control the convergence rate. The number of previous iterations $\tilde{L}$ used to predict the μ-value for the next iteration is 3 for all methods. Otherwise, the starting models and other settings are the same as for the previous test.

The resulting models (Fig. 5, Row 3) are now significantly closer to the synthetic model (Fig. 4, Row 1). Two high-velocity (high-density, high-resistivity) anomalies are present in the middle and the bottom of the model. Their positions (and the shape of the upper anomaly) fit well with the two layers representing the basalt and the basement. The region between the two layers has lower values of the physical properties and can be associated with the sub-basalt sediments. However, the presence of some artificial "egg-shaped" anomalies in this part of the model indicates the limits in resolution of the joint inversion. In addition, the objective functions of all three methods decrease at each individual iteration until the associated target misfit

is reached (Fig. 7d)) and final error weighted data fit from all three methods largely match the target misfit of 1.0 indicating a proper convergence behaviour. Only few iterations (2 and 4) are required to reach the target misfits for the gravity and seismic data, respectively, however many iterations (101) are required for MT. To some extent this slow convergence behaviour seems to be inherent to the synthetic model as already the individual MT inversion requires 45 iterations to reach the target misfit. Furthermore the criterion used in the joint inversion (i.e. $\Phi_{(d+m)}$ of the joint inversion with coupling constraint decreases only by a portion of the one of the unconstrained inversion) reduces the convergence speed compared to the individual MT inversions and for a value of $D^{MT} = 0.7$ one would expect that about $45/0.7 \approx 64$ iterations to be needed to reach the target misfit. One reason why almost double as many iterations are needed could be that the projection linking the individual physical models is far from an optimum and this slows down the overall inversion convergence.

In section 2.0.4 we discuss that the convergence behaviour may improve if the projection is controlled by the relative resolution power of the individual methods. Therefore we repeat the joint inversion test, but in this case the diagonal of the resolution matrix is used to weight the individual methods in the projection calculation (see section 2.0.4). Final results (compare Fig. 6, Row 1, with Fig. 5, Row 3) are very similar, however, the convergence for the MT method is 20% faster (compare Fig. 7d) and Fig. 7e)). In addition, the updates of μ^{MT} that are determined from the linear regression are now more reasonable (i.e. $\Phi_{(d+m)}^{MT,Constr.}$ decreases) for most iterations and a readjustment of μ^{MT} by using the loop ⓘⓥ (see Fig. 2) is only required for 2 iterations

572 (Fig. 7b)). In contrast, if the resolutions estimates are not considered in the
573 projection (Fig. 7a), μ^{MT} has to be readjusted for at approx. 30 iterations.
574 Based on these observations (and other synthetic examples not shown here),
575 convergence seems faster and more stable, if resolution is incorporated in the
576 calculation of the parameter projections.

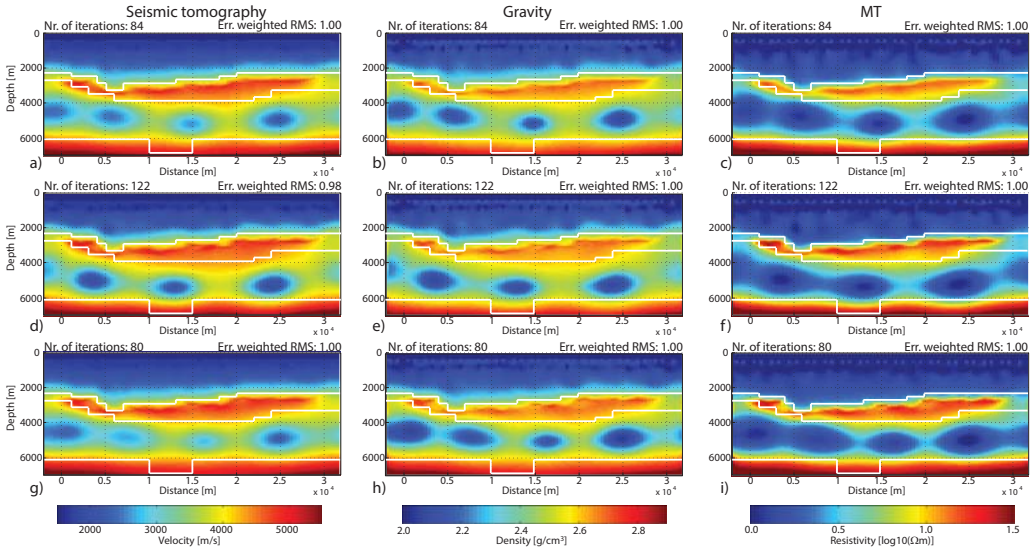

Figure 6: Final results from joint inversions, for which the strengths of coupling vary adaptively during the inversion process. For all tests shown here physical parameter projections are determined by considering relative resolution power of each method (see section 2.0.5). First and second row: Results from two tests, where different rates of adaption $D^{seis.} = D^{grav.} = D^{MT}$ of 0.7 and 0.4 are employed. Third row: Results from a test with other starting models (layered velocity model and homogenous half-space model for density $2.4 g/cm^3$ and resistivity of $10 \Omega m$). Otherwise the same parameters are employed as for the run, whose results are shown in the first row.

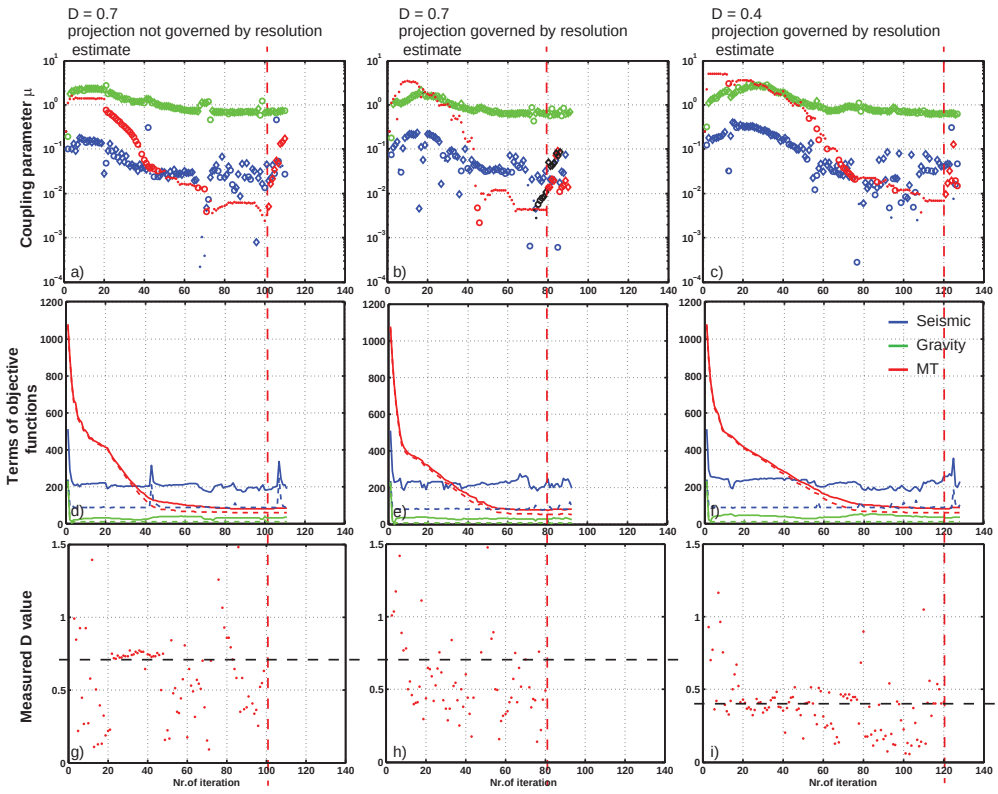

Figure 7: Behavior of the adaptive joint inversions from Figs. 5g)-i), Figs. 6a)-c) and Figs. 6d)-f) are shown in columns 1, 2 and 3, respectively. In all graphs blue refers to seismic, green to gravity and red to MT inversion parameters, shown as a function of iteration number. First row: Coupling parameters μ^{MT}, $\mu^{seis.}$ and $\mu^{grav.}$. The symbols ($\diamond$) and ($\circ$) indicate iterations, where the procedures III and IV (see Fig. 2) are active, respectively. Second row: Values of total objective functions (continuous lines) and their data terms (dashed lines). Third row: Ratio $\tilde{D}^{MT}$ of the incremental changes of the total objective functions for inversions without and with coupling constraints. This ratio is here only shown for the MT data, because the target misfits for the other methods are reached after very few iterations (< 5). Black dashed lines mark the associated pre-defined rate of adaption D^{MT}. Vertical red dashed lines indicate the iterations for which the target misfits are reached for all three methods.

For all adaptive joint inversions tests presented here, the inversion run is not terminated immediately after target misfits are reached for all methods, but continued for some additional iterations. As described in section 2.0.6, this strategy is adopted from Occam's inversion (see also loop ⓘⓥ in Fig. 2). Because three parameters (μ^{MT}, $\mu^{seis.}$, $\mu^{grav.}$) are adjusted simultaneously, it is difficult to find uniquely defined stopping criteria that reliably work for all types of models, methods and data sets. We therefore stop the joint inversion manually, when one of the coupling parameters shows a significant decrease for a few subsequent iterations. We generally observe that the model results are slightly better (i.e. in particular the physical properties of the basalt layer are higher and closer to the ones of the synthetic model) if the procedure is not terminated immediately after all target misfits are reached.

3.3.1. Impact of the parameters D onto the joint inversion behaviour

As discussed in section 2.0.5, the parameters D have in theory a large impact on the convergence speed for the associated methods. To investigate this in more detail, the previous joint inversion test is repeated with the same settings as before except for a lower value for $D^{seis.}$,$D^{grav.}$ and D^{MT} of 0.4. Obtained final models are very similar to the ones from the previous inversion run where $D = 0.7$ is used (Rows 1 and 2 in Fig. 6). However, as expected for decreased D values we require now significantly more iterations (120 compared to 81 iterations with higher D values) to reach the given target misfit (Fig. 7e) and f)). We also observe that the coupling parameter μ^{MT} has generally slightly higher values for a lower D^{MT} than for a larger D^{MT} values (Fig. 7b) and c)). This can be explained by the general behaviour of inversions that slower convergence correlates with stronger constraints.

3.3.2. Validation of the linear assumption of μ and Ψ

The linear assumption between the coupling parameters μ and the normalized changes in the objective functions Ψ in eq. 4 is intuitively made. Therefore we now test if it is appropriate and evaluate its effect on the efficiency of the joint inversion. The assumption can be considered as appropriate as long as the modified μ from the regression provide a convergent behaviour (i.e. a decrease of $\Phi_{(d+m)}^{Constr.}$). For our joint inversion runs, the MT part shows a convergent behaviour for most iterations (see small red dots in the Figs. 7a)-c)). Particularly the run, where we use large D-values of 0.7 and employ a resolution measure in the projection calculation, exhibits convergent behaviour for all but two iterations (see Fig. 7b and section 3.3).

To obtain a more quantitative measure to evaluate the validity of our assumption, we calculate for each method and for each iteration k:

$$\tilde{D} = \frac{\Delta\Phi_{(d+m)}^{Constr.,k}}{\Delta\Phi_{(d+m)}^{Ref.,k}}. \tag{9}$$

If the assumption is perfectly valid, $\tilde{D}$ would equal D. For the test run with $D^{MT} = 0.4$ we obtain a similar median of the $\tilde{D}^{MT}$ values of 0.378 and relatively low scatter of the $\tilde{D}^{MT}$ values with a $\sigma^2 = 0.042$ (Fig. 7i)), if we only consider D-values from iterations in which μ values are not modified by loop ⓘⓥ. It indicates that the linear regressions provide updates of coupling parameters which seem to satisfy the assumption. For a larger D^{MT}-value of 0.7, a larger discrepancy of the median value (0.508) and a larger variance of $\sigma^2 = 0.42$ suggest that the assumption is less appropriate (Fig. 7h). We have made several further tests with other D-values that confirm that a lower D-value results in a better controlled convergence behaviour.

At first glance, the better controlled convergence for low D-values appears to contradict the previous observation that convergence failed for fewer iterations when higher D-values are used. However, one has to consider that lower D-values (eq. 3) result in a slower convergence such that already a small scatter of the $\tilde{D}$-values can result in an increase of $\Phi_{(d+m)}^{Constr.}$ at any iteration. In summary, it is not easy to draw any general conclusions, for which D-values the assumption provides a convergent behaviour for most iterations. This is probably highly dependent on the methods involved and other settings of the actual inversion.

3.3.3. Dependence of the starting model

We repeat the joint inversion test with $D^{seis.} = D^{grav.} = D^{MT} = 0.7$ with different starting models, which are not linked by the parameter relationships and are further away from the synthetic model. Homogenous half-space models with $2.4 g/cm^3$ and $10 \Omega m$ are chosen for the gravity and MT inversions, respectively, and a layered velocity model is taken for the seismic inversion. Final results are similar to the ones from the joint inversion having the same parameter settings, but starting models that are linked by parameter relationships (see section 3.3) (compare the Rows 1 and 3 in Fig. 6). Convergence speed of gravity and seismic inversion is similar, but MT inversion reaches the target misfit even faster after 67 iterations compared to 81 iterations.

The choice of the starting model seems not critical for conditions, where the total resolution of the joint inversion is rather high and all models explaining the data are similar. We attribute this to the observation that adaption of the coupling strengths reduces the risk that the inversions get stuck in a local minima.

3.4. Results from joint inversions using both petrophysical and structural information

To further improve the results from the petrophysical inversion we now add structural information. First, we test a purely structural joint inversion using the mutual cross-coupling strategy described in the methodological section 2.0.7. The weights applied to the discrete derivative matrix $\mathbf{C}$ are calculated using values of 0.1 and 1.0 for the parameters α and β in eq. 7, respectively. As starting models the same linked parameter models are used as described before.

This joint inversion run gets stuck in some local minima and misfits for seismic (minimum $d_{RMS}^{seis.} = 4.72$) and MT (minimum $d_{RMS}^{MT} = 2.64$) and do not reach the target misfits. We conclude that starting models close to the synthetic models are required to such that this approach is successful. And although our starting models are derived from the final results of the individual inversions they are still too inaccurate to provide conditions for the structural joint inversion to converge. We note that other studies using this coupling strategy successfully combine geophysical methods with higher resolutions (e.g. seismic tomographic and electrical resistance tomography, Günther and Rücker, 2006), where the starting models obtained from individual inversions are close enough to the true subsurface conditions to ensure convergence of the joint inversion.

Based on this observation, we choose as starting models for the combined structural and petrophysical joint inversion the models from the 72th iteration of the adaptive joint inversion with $D^{seis.} = D^{grav.} = D^{MT} = 0.7$ and a resolution measure in the projection calculation. In all three parameter

models locations of main anomalies are overlapping such that it can be assumed that these starting models are close enough to the synthetic model for the inversion to converge. Target misfits for all methods are reached after few iterations (< 6 for all methods). The coupling parameters are generally slightly higher than for the corresponding purely petrophysical joint inversion (see black symbols in Fig. 7b), probably due to the fact that overall smoothing is reduced by cross-coupling such that more coupling is required to obtain the same data misfits as for the inversion without structural linkage.

Final results (Fig. 8) show that this combined structural and petrophysical joint inversion resolves the main structures as well as the purely petrophysically coupled joint inversion. However, the boundary between the upper sediments and the basalt is now sharpened in all three parameter models (compare with results in Fig. 6) and its location coincides well with upper sediments-basalt interface in the synthetic model. This demonstrates that a combination of both structural and petrophysical linkage further improves joint inversion results.

4. Real data example

We apply our joint inversion scheme to data recorded about 150 km southeast of the Faroe Islands (Fig. 9). This area is characterized by thick sequences of basalt flows that are associated with magmatic activity during the continental break-up of the North Atlantic in the Tertiary (e.g. White et al., 2003; Gallagher and Dromgoole, 2007). The basalt flows overlie sediments accumulated in basins during earlier episodes of stretching of the continental lithosphere from the late Carboniferous to the early Paleocene.

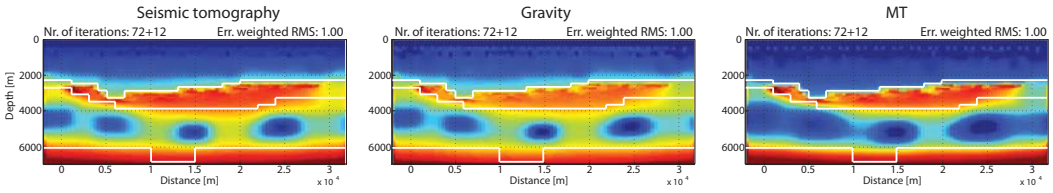

Figure 8: Final results for a joint inversion, which combines the adaptive coupling strategy considering petrophysical information with mutual cross-coupling strategy considering structural information. Starting models for this run are the intermediate results (72 iteration) of the petrophysical inversion, whose results are shown in Figure 6. For this inversion D values are set to 0.7 and resolution estimated are incorporated in the calculation of physical parameter projections.

Traps in these Mesozoic sub-basalt sediments are considered as potential hydrocarbon-bearing structures. Underneath the sediments a pre-rifted basement is present which probably consists of gneissic rocks and formed during the Caledonian Orogeny.

In this area comprehensive geophysical data sets are available for a wide-range of methods. *Statoil*, who manages License L006 (red outline in Fig. 9) in this region, provided us with geophysical data presented here. The data include a pattern of wide-angle seismic lines, a marine 3-D Full Tensor Gravity (FTG) survey and a number of MT sites distributed on a 3-D grid. While the data provide 3-D coverage, we limit our investigation to 2-D lines, since *JINV2D* cannot handle 3-D MT data. We therefore focus on the FLA6 profile, which crosses the northern part of the license area in WNW-ESE direction (green line in Fig. 9). Hence in the joint inversion presented here we only use seismic data from FLA6 (49093 seismic first arrival times from shot gathers that have offset ranges of 3 to 18km) and gravity (425 locations

714 from a 3-D shipborne survey) and MT data (11 stations with periods from
715 0.0061 to 0.15 s) that are measured in the vicinity of this profile.

716 Data from the individual methods were collected in separate surveys from
717 1995 to 2002 and the acquisition strategies are not optimized for such data
718 integration. MT stations used in our 2-D joint inversion are not located
719 immediately on the seismic profile but lie up to 7 km on either side of it.
720 MT and gravity data only overlap with seismic data in the western and
721 eastern part of the profile (Fig. 9), respectively. In addition to the geophysical
722 data used for the inversion, we received data from a 3-D reflection seismic
723 survey, which has a large overlap with the FLA6 profile in the northern
724 part of the licence, and logging data from the 4200 m deep BRUGDAN well
725 located in the immediate vicinity of the FLA6 profile (red star in Fig. 9).
726 The reflection seismic data allow a direct comparison of the joint inversion
727 results with structures derived independently. We use the logging data (sonic,
728 resistivity and gamma-gamma log) to derive parameter relationships for our
729 joint inversion, which are depth independent.

730 The nearly vertical BRUGDAN borehole penetrates the top basalt and
731 the underlying sediments at 1154m and 3719m below sealevel, respectively
732 (Schuler et al., 2012). Logging data show a distinct increase in P-wave veloc-
733 ities and resistvities across the upper sediment-basalt interface (see Fig. 10).
734 (Although no density data from logging are available above the basalt, it is
735 likely that densities of the basalt are significantly higher than of the shallow
736 sediments.) The possible base of the basalt sequence is however character-
737 ized by a more gradual change in physical parameters. Figures 11a) and b)
738 show cross-plots and we observe that there are positive correlations between

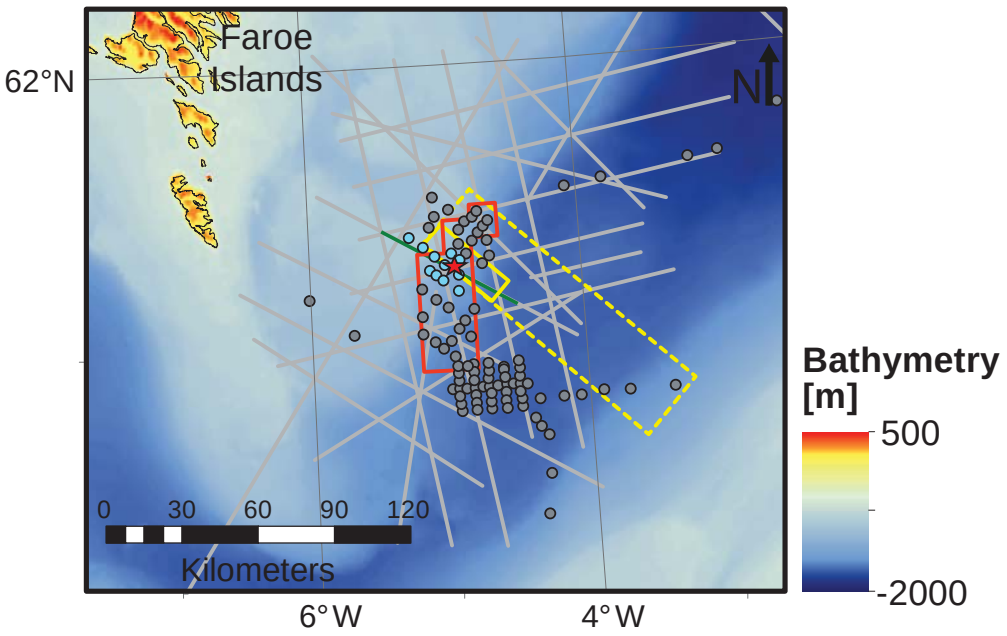

Figure 9: Map of our investigation area in the Faroe-Shetland Basin. A FTG survey (dashed yellow rectangle), several wide angle seismic profiles (grey lines) and MT sites (circles) are present in the region. Data used in our 2-D joint inversion along the seismic profile FLA6 are highlighted (small yellow rectangle, green line and light blue circles correspond to the gravity, seismic and MT data, respectively). Red star indicates the position of the BRUGDAN borehole, red line outline the license area L006.

seismic P-wave velocity and resistivity and between P-wave velocity and bulk density. Such positive v_p-d correlations are present for many subsurface conditions, but positive v_p-ρ correlations are less common and are reported for fewer geological conditions e.g. for sub-basalt regions due to the effect of the pore space on both v_p and ρ (e.g. Jegen et al., 2009).

To estimate adequate parameter relationships for the joint inversion, curve-fitting in a least-square sense was performed between the physical prop-

erties of the borehole logging data (Fig. 11a)-b)). The analytic expressions are

$$\log_{10} \rho = 7.876 \cdot 10^{-8} \cdot (v_p)^2 - 0.1512$$

$$d = 0.0001737 \cdot v_p + 1.868$$

for the velocity (in m/s) - resistivity (in Ωm) and velocity (in m/s) - density (in g/cm^3) relationships, respectively.

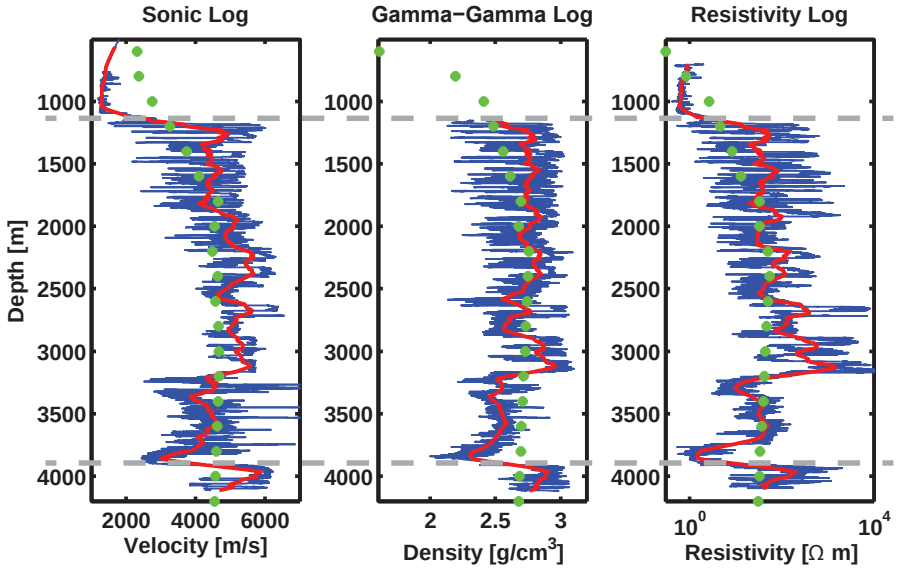

Figure 10: Comparison of the logging data from the BRUGDAN borehole and the joint inversion results along the prole FLA6. Blues lines show measured borehole logs and red lines the same data after applying a moving average (filter length = 100 m). Green dots indicate the physical properties obtained from the joint inversion along the borehole drilling (see Fig. 17). Horizontal grey dashed lines indicate top and base basalt as proposed by Schuler et al. (2012).

The logging data generally show a large variation of the physical properties on a sub-metre scale. Cross plots of the physical parameters (Fig. 11) show that this results in a larger scatter around the fitted relationships and reveal that for some geological structures rock property links are systematically shifted (e.g. depth range 2500-3150 m in Fig. 11a-b) such that the fits are not good representations for these depths ranges. However, if the logging data are averaged over depths intervals of $100m$, which corresponds to the cells widths in the inversion, the relationships are adequate estimates for the scale resolvable by the inversions (Fig. 11c-d)).

4.1. Estimation of data errors

It is crucial for our adaptive joint inversion scheme to use realistic data error estimates, as the coupling strength of a method is strongly dependent on the level of the associated target misfit (at later iterations when the loop ⓜ in Fig. 2 becomes relevant). For seismic and gravity we estimated errors directly from the available data. For a number of seismic shot gathers first-arrivals were picked independently by three experienced persons. A meaningful offset dependent error estimates for all seismic data is derived by considering the time variations of the three picked onsets for the same traces. For the gravity the data spacing of measurement points in the in-line direction is small ($\approx 15m$) and the ocean is several hundred meters deep such that variations with short wavelength can be associated with uncorrelated noise. We therefore obtain a proper error estimate ($\sigma^2 = 0.1mgal$) through experimental variograms at very small distances ("nugget" effect; see e.g. Dubrule, 2003). For MT we only received processed data as frequency dependent impedance estimates together with some error estimates (determined by a robust pro-

cessing scheme), but not the original time series of the electromagnetic field components. Hence, we cannot determine any error estimates ourselves or to evaluate the reliability of the error estimates provided. When we perform the inversions (both a single MT inversion and the adaptive joint inversion), it is not possible to reach the proposed target misfits for MT even with fine gridding. Dimensionality analysis indicates that the resistivity distribution are either 1-D or 2-D (with the strike oriented perpendicular to the profile direction), so 3-D effects can be largely excluded as the cause for high misfits, which leads us to conclude that errors are generally underestimated. We therefore choose for the joint inversion target misfits that are similar to the minimum misfits we obtain from single MT inversions. During the joint inversion we observe (see discussion below) that coupling parameters of the MT are not extremely low for the chosen target misfit and that the results are generally meaningful indicating that the chosen target misfit is appropriate.

4.2. Parameters used for the joint inversion

The model consists of 68 and 71 inversions cells in x- and z-direction, respectively, with a constant cell size of 0.5×0.1 km. Starting models for the gravity and MT inversion have constant densities and resistivities of $d = 2.5 g/cm^3$ and $\rho = 10 \Omega m$ below a high conductive and low-density layer associated with the seawater column of the ocean. The velocities of the seismic starting model gradually increase with depth from $1500 m/s$ at the sea-bottom to $6000 m/s$ at 4000 m depth. As for the synthetic tests, the coupling strengths vary adaptively during the joint inversion procedure. To control the convergence speed $D^{seis.}$, $D^{grav.}$ and D^{MT} of 0.4 are chosen and $\tilde{L} = 3$ iterations are used for each method to modify the μ-value

for a subsequent iteration. The coupling parameters at the first iterations are set to $\mu^{seis.} = \mu^{grav.} = \mu^{MT} = 0.25$. The calculation of the projection is governed by resolution estimates as already described above and the regularisation parameters λ are gradually reduced from starting values of $\lambda^{seis.} = \lambda^{grav.} = \lambda^{MT} = 0.25$ by using the method proposed by Lelièvre et al. (2012). Structural cross-coupling is only used for the last iterations (> 60).

4.3. Joint inversion results

The convergence behaviour for all three methods (see Fig. 12) is stable and target misfits for gravity, seismic and MT are reached after 3, 13 and 60 iterations, respectively. Similar observed data and calculated data from the joint inversion (see Figures 13, 14 and 15) indicate that the data are well-fitted for all methods. The final parameter models from this joint inversion run are shown in Fig. 16, Row 2. To evaluate the improvements obtained by using our joint inversion strategy, we perform corresponding separate inversion with similar parameters as for the joint inversion (same starting models, same inversion grid, similar regularization strength). It is obvious that the joint inversion results are more consistent with each other than the results from the individual inversions (compare Row 1 and Row 2 of Fig. 16). In the joint inversion models low v_p, d and ρ values at shallow depths are separated by a sharp boundary from quasi horizontal high velocity, high density and high resistivity anomalies present in a depth range from about 2000 to 4000 m. Below 4000 m the physical parameters gradually decrease again with depth. These anomaly distributions are associated with a basaltic sequence enclosed by sediments above and below. In contrast, the single seismic inversion resolves only well the upper sediments and top

basalt, but no structures underneath. The single MT inversion creates a mostly horizontal high-resistive layer in the western and central part of the profile that is covered by MT stations. The anomaly is, however, too thick to realistically represent the basaltic sequence. The horizontal density anomaly from the single gravity inversion results is not well resolved and is largely dependent on the chosen starting model.

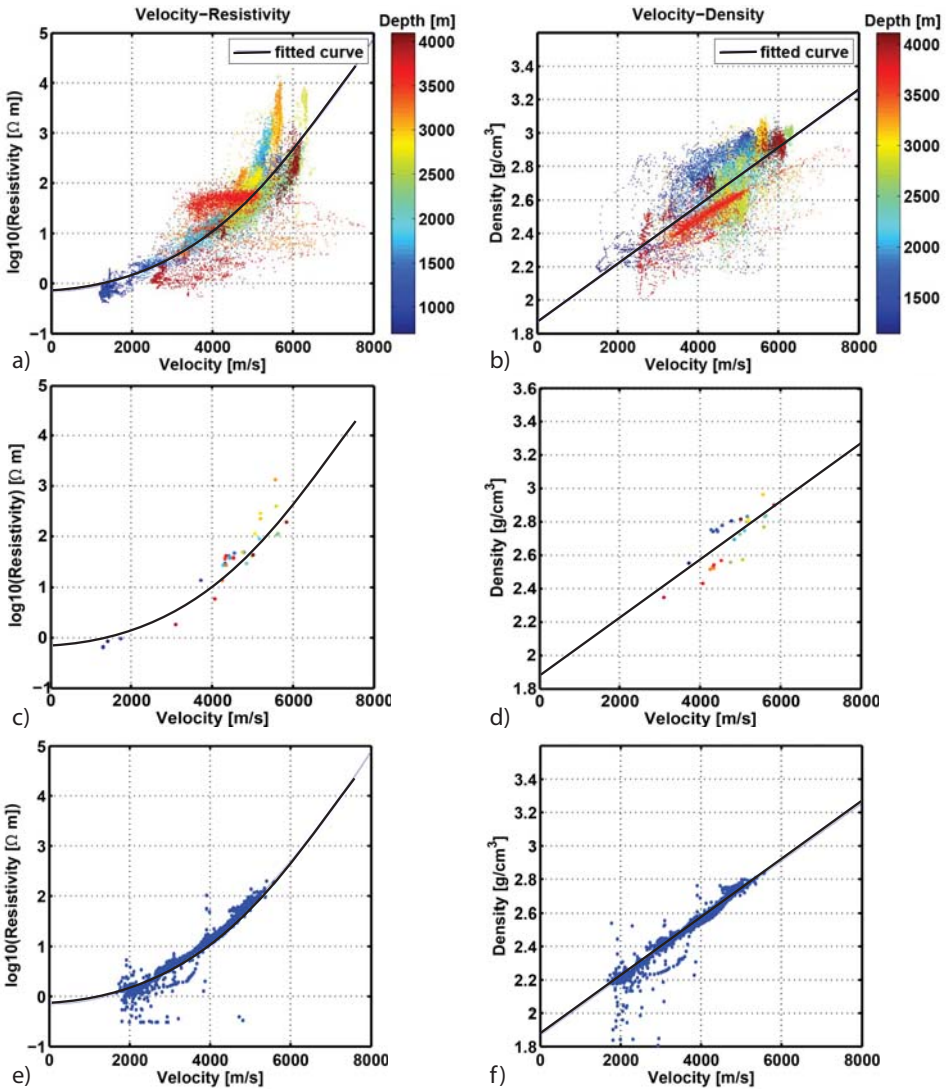

Figure 11: a) and b): Cross plots of the logging data from the borehole BRUGDAN. Color-coding of the dots is associated with the actual depths. c) and d): Mean values of physical properties calculated for 100 meter intervals and presented in the same form as for a) and b). e) and f): Cross plots for the final results of the adaptive joint inversion. Black lines show parameter relationships determined by fitting of logging data, which are used in our joint inversions.

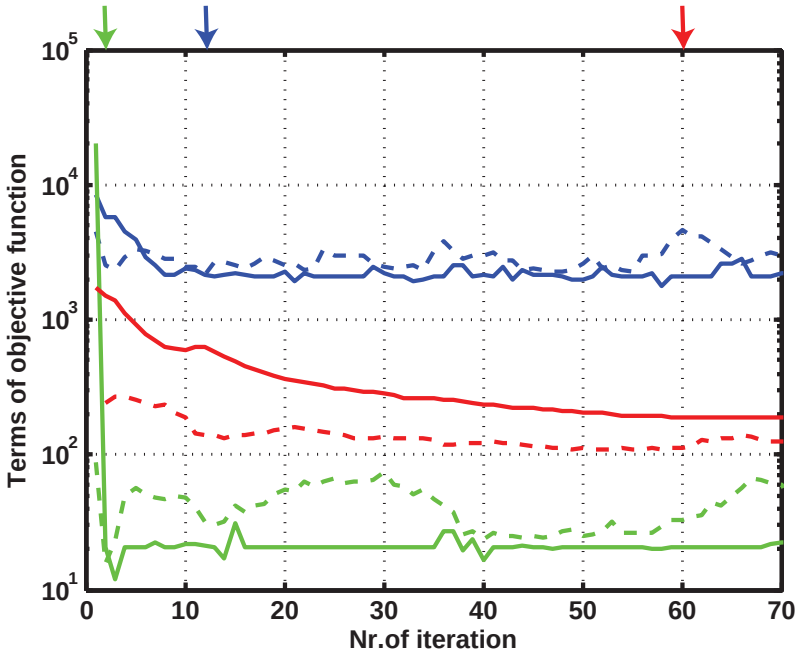

Figure 12: Convergence of our adaptive joint inversion for real data example. Values of data and regularization terms of the objective functions are plotted as continuous and dashed lines, respectively. Seismic data, gravity data and MT data are shown in blue, green and red, respectively. Arrows indicate iterations at which target misfits for the associated methods are reached.

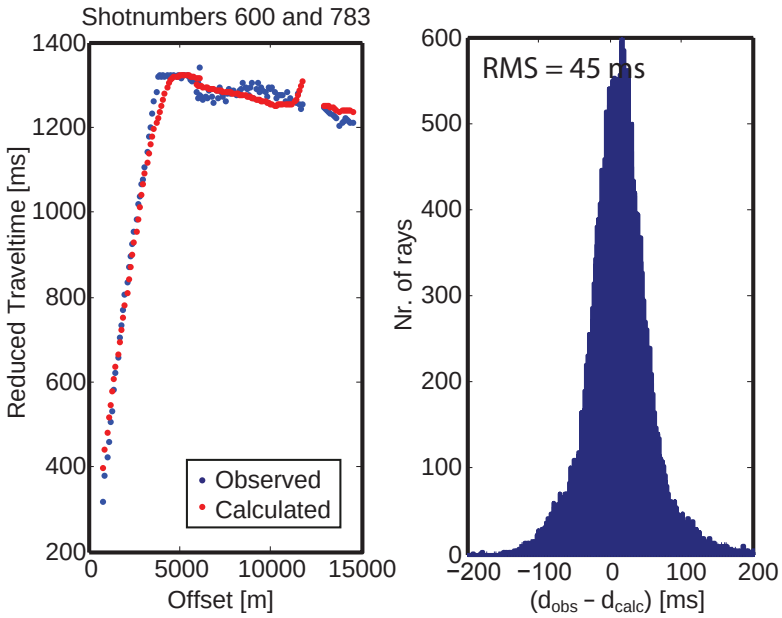

Figure 13: Final seismic data misfits for the adaptive joint inversion. Left: Picked first arrival times (red) for a typical shot gather together with the corresponding calculated traveltimes (blue). Traveltimes in the shot gather are reduced with a velocity of 5000 m/s, Right: Histogram of data misfits from all seismic first arrival times used in joint inversion.

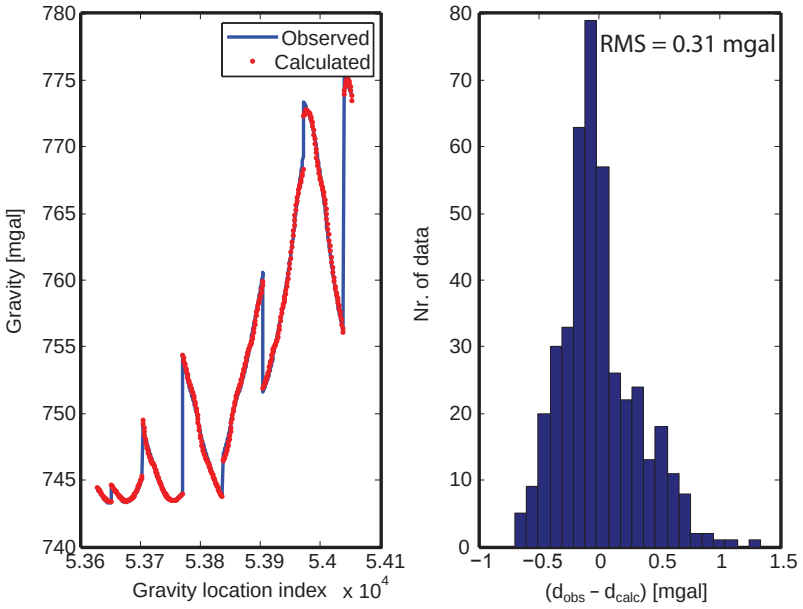

Figure 14: Final gravity data misfits for the adaptive joint inversion. Left: Observed (blue) and calculated (red) gravity responses for all measuring points. Right: Histogram of the gravity data misfits.

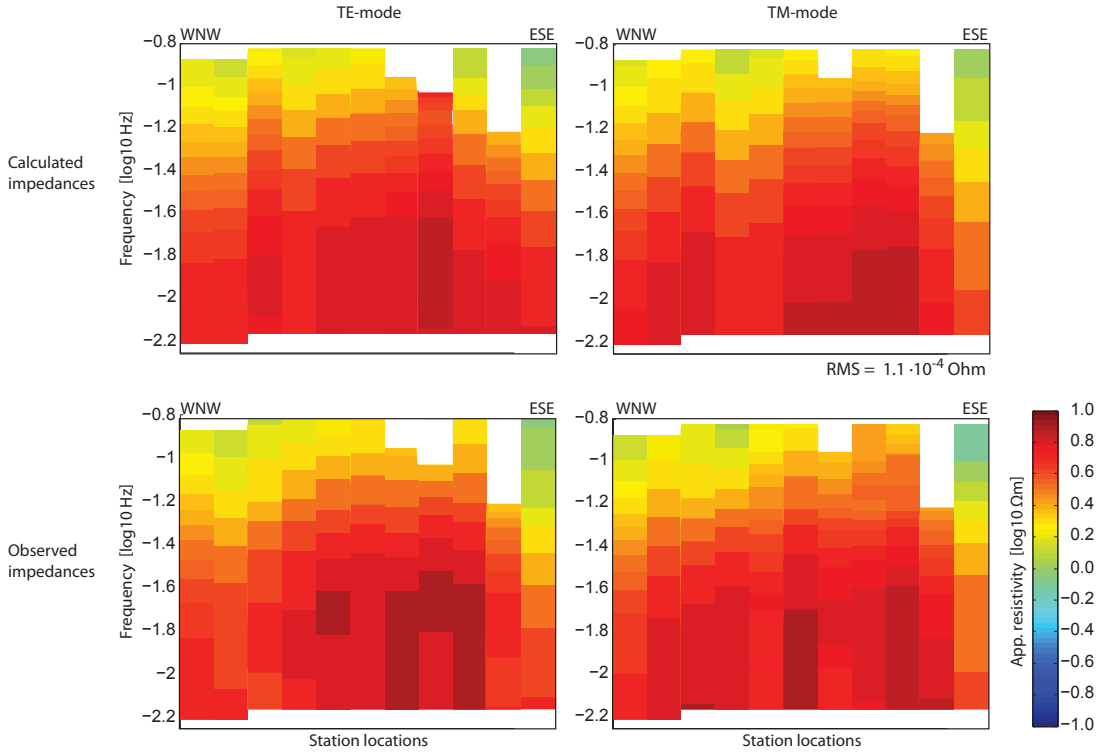

Figure 15: Final MT responses obtained from the adaptive joint inversion. Apparent resistivities for all frequencies and stations are shown for the calculated (top panels) and observed (bottom panels) responses for TE mode (left) and TM mode (right) polarization.

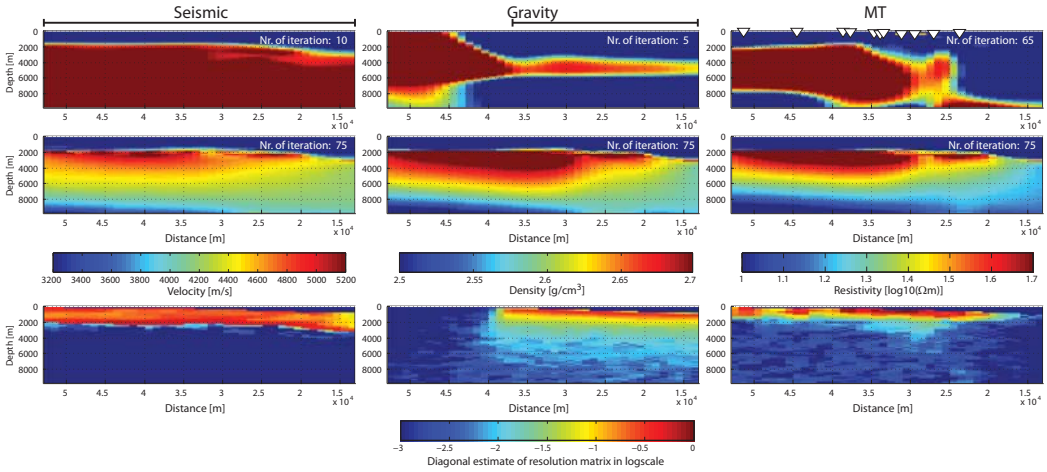

Figure 16: Inversion results and resolution estimates for the seismic, gravity and MT data used for the real data example. First and second row show the results from separate inversions and adaptive joint inversion. Black lines above the velocity model and density model indicate areas, where seismic and gravity data were acquired. Triangles above the resistivity model mark the positions of the marine MT sites. Third row shows approximations of the diagonal elements of the resolution matrices for the final models of the joint inversion (second row).

Although the results from joint inversion are consistent, the total resolution below the top basalt is relatively low for all methods (see diagonal estimates of the resolution matrices in Fig, 16, Row 3). Lack of measurement sites for gravity and MT at the west and east side of the profile result in a strongly reduced resolution in these areas. This indicates that a more complete coverage and the use of other data; e.g. seismic reflection onsets in the seismic (Fliedner and White, 2003) or CSEM (Panzner et al., 2014; Hoversten et al., 2015) could further improve the results particularly at larger depths.

As mentioned above the physical parameter relationships are only estimates which are not valid everywhere and we indeed observe decoupling in some parts. Coupling parameters are with $\mu^{seis.} = 0.0010$ - 0.0227 and $\mu^{MT} = 0.045$ - 0.212 low for seismic and MT at the late iterations (60 to 65) - only $\mu^{grav.}$ has higher values ranging from 0.33 to 0.45, and cross-plots of the physical parameters of the final joint inversion results (Fig. 11e-f) show distinct deviations from the relationships for a number of inversion cells.

To verify our joint inversion results we compare the joint inversion models with 3-D reflection seismic data and borehole data. Since the z-axis of the reflection seismic data set is given in time and not in depth, the final joint inversion models are converted to two-way travel-times by using the velocity model obtained from the joint inversion. In Figure 17 the resultant resistivity model is shown together with the cross-section of the 3-D seismic data cube along the FLA6 profile. Although both, resistivity and the seismic model, have some uncertainty, the top basalt reflection in the seismic data coincides well with the sharp boundary between low resistivities

associated with the shallow sediments and high resistivities associated with the basalt. It demonstrates that joint inversion provides accurate results in the well-resolved shallow part. Comparison in the deeper part is much more difficult because both reflection seismic and joint inversion give less clear results. A distinct seismic reflection associated with the base basalt is absent, but instead there is a pattern of discontinuous reflections that is interpreted as the base basalt (see dashed line in Fig. 17). The data from the bottom of the BRUGDAN borehole (Schuler et al., 2012) and results from wide-angle seismic studies (Fliedner and White, 2003; Spitzer et al., 2003) support this interpretation. Resolution of the joint inversion is significantly reduced at this depth range resulting in smooth changes in the parameter models. To evaluate if the thickness and, hence, the lower bound of the horizontal anomalies with large physical properties representing the basalt layer ($v_p > 4500m/s$ and $\rho > 30\Omega m$) are reliable, we repeat the joint inversion with different starting models. Results show that thicknesses of anomalies are generally stable for most of the western and the central part, but not in the eastern part which is not covered by MT sites. Comparison of the joint inversion models with the logging data as a function from depth shows that the modelled physical parameters are in the same range as the logging data for both the upper sediments and the basalt, however, variations within the basaltic sequence are not resolved (Fig. 10).

Other studies based on seismic data note that a NE-SW striking structural high of the pre-rifted basement - the East Faroe High - rises in the vicinity of the BRUGDAN borehole and the white arrows in Figure 17 may indicate reflections associated with this structure. However, in the joint inversion

model no such structure is observed, which we attribute to the fact that the resolution of the methods combined in the joint inversion is not high enough to resolve the deep basement.

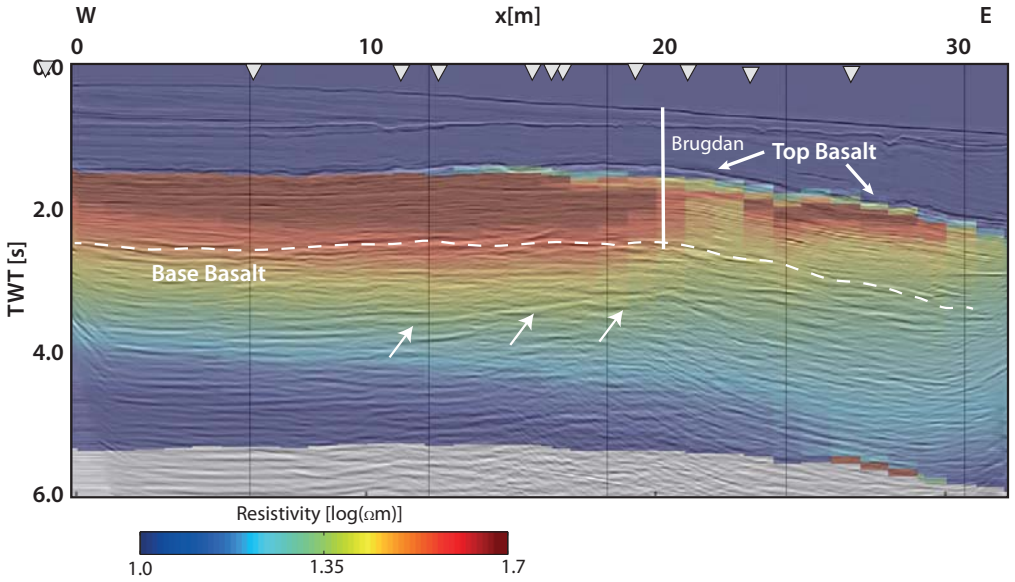

Figure 17: The transparent resistivity image from the joint inversion superimposes the cross-section from the 3-D reflection seismic dataset along the FLA6 profile (see Fig. 9). To transfer the depth axis of the resistivity image to two-way-travel times, the final velocity model from the joint inversion is used. Triangles indicate the locations of MT stations and dashed lines show the basalt as proposed by reflections seismic and logging data from the BRUGDAN borehole. Arrows highlight some reflectors associated with the pre-rifted basement.

5. Conclusion and Outlook

We have demonstrated that critical issues associated with joint inversion algorithms are handled in our joint inversion scheme: 1)a petrophysical joint inversion, in which parameter relationships are considered as constraints, requires no relative weighting of the data sets; 2) both for the synthetic tests and in the real data example, we observe that the implemented adaption of the coupling parameters makes the convergence of the individual methods robust and independent of the choice of parameters controlling the joint inversion as the adaption rates D. For all runs with the adaptive joint inversion, the target misfits are reached for all methods and results are close to the true models; 3) by considering the spatially dependent resolution power of the individual methods in the coupling constraints, the convergence behaviour is improved compared to the same joint inversion where resolution estimates are not incorporated; 4) results from the real data example show that the obtained rock property behaviour can deviate from the assumed parameter relationships used as constraints. This happens when the true rock properties are, in parts, not adequately represented by the relationships and a too strong coupling is in disagreement with low data misfits.

In addition to these critical issues, we have shown that also structural information can be easily incorporated in this otherwise petrophysically linked joint inversion scheme by adjusting the smoothing constraints by mutual cross-coupling. Such added structural information sharpens parameter boundaries in parts of the models that are well resolved for some of the geophysical methods used.

Application of the adaptive joint inversion scheme on a combined wide-

angle seismic, MT and gravity data set that was acquired offshore the Faroe Islands, a region that is characterized by large-scaled flood basalt, demonstrates that this joint inversion works reliably also for real data and provides more consistent results than individual inversions. However, the same results indicate that even the combination of these methods is unable to adequately resolve deep structures such as thickness of the sub-basalt sediments and the pre-rifted basement. This is not directly related to our joint inversion strategy but to the low resolution power of the methods in the deeper subsurface. To resolve sub-basalt structures more complete coverage and possibly other geophysical data are required. For example we recommend to use reflection events in the seismic tomography and to add CSEM as another electromagnetic method (Panzner et al., 2014; Hoversten et al., 2015) in the future.

6. ACKNOWLEDGMENTS

We thank *Wintershall* and the *SINDRI* consortium for sponsoring the research position of Björn Heincke and part of this project (project number C46-54-01). We thank Bernd Lahmeyer (*Statoil*, Stavanger), Christian Berndt (*GEOMAR*, Kiel) and an anonymous reviewer for helpful comments. David Bösing (*Baker&Hughes*, Celle) supported this work by evaluating different resolution estimates. *Statoil* provided us the field data used in this study.

Appendix A. Projection method

Given a point P, consisting of the n physical parameters $m^{(1)}, ..., m^{(n)}$, we use an iterative method to determine a projection $\tilde{P} = (\tilde{m}^{(1)}, ..., \tilde{m}^{(n)})$ onto a

pre-defined relationship curve. Convergence of this method is assured as long as the relationship curve is strictly monotonic. Although only two physical parameters are used in the following example (Fig. A.18), we emphasize that the method is in general not limited by the number of considered physical parameters.

In the first iteration of the procedure, lines parallel to the x- and y-axis that pass through the point $P = (m^{(1)}, m^{(2)})$ are determined (Fig. A.18a). For these lines, the points of intersection $A = (m^{(1)}_{A,1}, m^{(2)}_{A,1})$ and $B = (m^{(1)}_{B,1}, m^{(2)}_{B,1})$ with the relationship curve are determined and the mean values $m^{(1)}_{AB,1} = \frac{m^{(1)}_{A,1}+m^{(1)}_{B,1}}{2}$ and $m^{(2)}_{AB,1} = \frac{m^{(2)}_{A,1}+m^{(2)}_{B,1}}{2}$ are calculated. For the next iteration axis parallel lines passing through $m^{(1)}_{AB,1}$ and $m^{(2)}_{AB,1}$ are then used to determine new points of intersection with the relationship curve $(m^{(1)}_{A,2}, m^{(2)}_{A,2})$ and $(m^{(1)}_{B,2}, m^{(2)}_{B,2})$ (Fig. A.18b). From these points again the mean values $m^{(1)}_{AB,2} = \frac{m^{(1)}_{A,2}+m^{(1)}_{B,2}}{2}$ and $m^{(2)}_{AB,2} = \frac{m^{(2)}_{A,2}+m^{(2)}_{B,2}}{2}$ are determined.

At every iteration the two points of intersection converge against each other. If the distance between the intersections points becomes smaller than a pre-defined threshold value at the t-th iteration the procedure is stopped. The mean values of the points of intersection $(\frac{m^{(1)}_{A,t}+m^{(1)}_{B,t}}{2}, \frac{m^{(2)}_{A,t}+m^{(2)}_{B,t}}{2})$ is then considered as the projection point $\tilde{P} = (\tilde{m}^{(1)}, \tilde{m}^{(2)})$.

Because $m^{(1)}_{AB}$ and $m^{(2)}_{AB}$ depend on variations of the first and second physical parameter, respectively, the influence of the different parameters is inherently balanced and, hence, more or less independent of employed units and slope of the relationship curve.

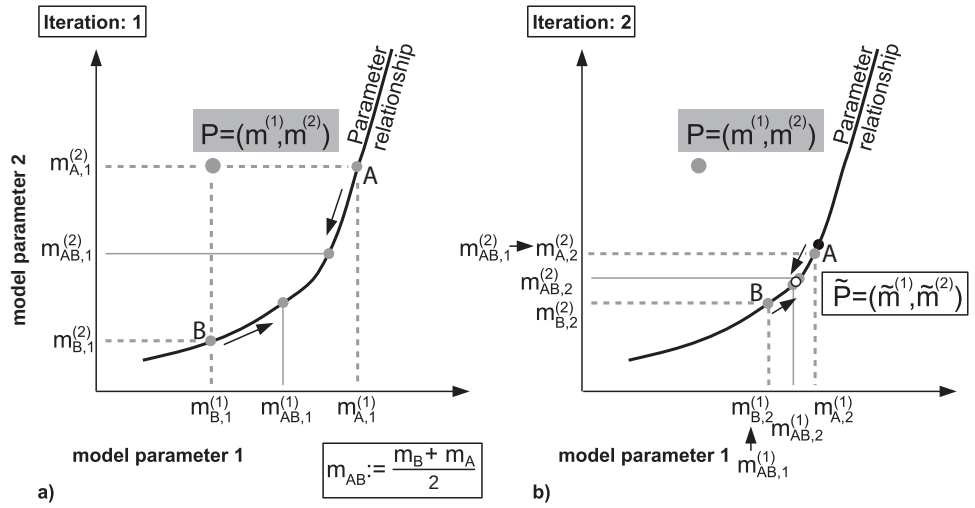

Figure A.18: Sketch illustrating the iterative procedure to determine for a point of two physical parameters $m^{(1)}$ and $m^{(2)}$ a projection $(\tilde{m}^{(1)}, \tilde{m}^{(2)})$ onto a relationship curve. (a) and (b) show the 1st and 2nd iteration step of the procedure assuming that both parameters are equally weighted. The white and black dot in b) show the obtained projection point if the same weights and different weights of $\psi = 1.0$ and $\phi = 0.5$ are considered for the two parameters (see Appendix B), respectively.

Appendix B. Modification of the projection to account for the model resolutions

The general procedure is the same as already described as in the Appendix A. However, the sums $m^{(1)}_{AB,t}$ and $m^{(2)}_{AB,t}$ are now calculated by some weighted mean values. In the case of having two parameters and using the diagonal elements $d^{(1)}$ and $d^{(2)}$ of the resolution matrix as measures, they are obtained as:

$$
\begin{aligned}
m^{(1)}_{AB,t} &= \frac{\psi m^{(1)}_{A,t} + \phi m^{(1)}_{B,t}}{|\psi| + |\phi|} \\
m^{(2)}_{AB,t} &= \frac{\psi m^{(2)}_{A,t} + \phi m^{(2)}_{B,t}}{|\psi| + |\phi|} \\
\text{with} \quad & \psi = 1.0 - |1.0 - d^{(1)}| \quad \text{if } \gamma \leq d^{(1)} \leq 2.0 \\
& \psi = \gamma \qquad\qquad\qquad\quad \text{otherwise} \\
\text{with} \quad & \phi = 1.0 - |1.0 - d^{(2)}| \quad \text{if } \gamma \leq d^{(2)} \leq 2.0 \\
& \phi = \gamma \qquad\qquad\qquad\quad \text{otherwise}
\end{aligned}
$$

γ is a small positive value (we use in all test $\gamma = 0.002$) that is introduced to make the determination of the projection direction less sensitive to inaccurate calculation of the diagonal element estimates of the resolution matrix.

The black dot in Figure A.18b shows the projection point for weights of $\psi = 1.0$ and $\phi = 0.5$.

References

M. Moorkamp, P. Lelievre, N. Linde, A. Khan (Eds.), Integrated Imaging of the Earth, AGU-Wiley, 2016.

P. Xu, Iterative generalized cross-validation for fusing heteroscedastic data of inverse ill-posed problems, Geophys J. Int. 179 (2009) 182–200.

A. Abubakar, M. Li, J. Liu, T. Habashy, Simultaneous joint inversion of MT and CSEM data using a multiplicative cost-function, in: SEG Technical Program Expanded Abstracts, Houston, USA, vol. 29, 719–723, 2009.

T. Günther, C. Rücker, A new joint inversion approach applied to the combined tomography of DC resistivity and seismic refraction data., in: Expanded Abstract for 19. EEGS annual meeting (SAGEEP), Seattle, USA, 2006.

H. Paasche, J. Tronicke, Cooperative inversion of 2D geophysical data sets: A zonal approach based on fuzzy c-means cluster analysis, Geophysics 72 (2007) A35–A39.

A. Bouchedda, M. Chouteau, A. Binley, B. Giroux, 2-D joint inversion of cross-hole electrical resistance and ground penetrating radar data, Journal of Applied Geophysics 78 (2012) 52–67.

T. Zhu, J. M. Harris, Improved estimation of P-wave velocity, S-wave velocity, and attenuation factor by iterative structural joint inversion of crosswell seismic data, Journal of Applied Geophysics 123 (2015) 71 –80.

M. E. Kilmer, D. P. O'Leary, Choosing regularization parameters in iterative methods for ill-posed problems, SIAM J. Matrix Anal. Appl. 22 (2001) 1204–1221.

C. R. Vogel, Computational Methods for Inverse Problems, Frontiers in applied mathematics. Society for Industrial and Applied Mathematics, 2002.

P. C. Hansen, Analysis of discrete ill-posed problems by means of the L-curve, SIAM Review 34 (1993) 561–580.

G. H. Golub, C. F. Van Loan, Matrix Computations, John Hopkins University Press, Baltimore, 3 edn., 1996.

V. A. Morozov, On the solution of functional equations by the method of regularization, Soviet mathematics - Doklady 7 (1966) 414 – 417.

P. G. Lelièvre, C. G. Farquharson, C. A. Hurich, Joint inversion of seismic traveltimes and gravity data on unstructured grids with application to mineral exploration, Geophysics 77 (2012) K1–K15.

L. A. Gallardo, M. A. Meju, Joint two-dimensional DC resistivity and seismic travel time inversion inversion with cross-gradients cross constraints, Journal of Geophysical Research 109 (2004) B03311.

L. A. Gallardo, Multiple cross-gradient joint inversion for geospectral imaging, Geophysical Research Letters 34 (2007) L19301.

M. Lien, Simultaneous joint inversion of amplitude-versus-offset and controlled-source electromagnetic data by implicit representation of common parameter structure, Geophysics 78 (2013) ID15–ID27.

E. Haber, D. Oldenburg, Joint inversion: a structural approach, Inverse Problems 13 (1997) 63–77.

J. Doetsch, N. Linde, A. Binley, Structural joint inversion of time-lapse crosshole ERT and GPR traveltime data, Geophysical Research Letters 37 (2010) L24404.

D. M. Molodtsov, V. N. Troyan, Y. V. Roslov, A. Zerilli, Joint inversion of seismic traveltimes and magnetotelluric data with a directed structural constraint, Geophysical Prospecting 61 (2013) 1218–1228.

M. Moorkamp, A. W. Roberts, M. Jegen, B. Heincke, R. W. Hobbs, Verification of velocity-resistivity relationships derived from structural joint inversion with borehole data, Geophysical Research Letters 40 (2013) 3596–3601.

J. M. Lees, J. C. VanDecar, Seismic tomography constrained Bouguer gravity anomalies: Applications in western Washington, Pure and Applied Geophysics 135 (1991) 31–52.

Afnimar, K. Koktsu, K. Nakagawa, Joint inversion of refraction and gravity data for the three-dimensional topography of a sediment-basement interface, Geophysical Journal International 151 (2002) 243–254.

M. Moorkamp, B. Heincke, M. Jegen, A. W. Roberts, R. W. Hobbs, A framework for 3-D joint inversion of MT, gravity and seismic refraction data, Geophysical Journal International 184 (2011) 477–493.

D. Colombo, M. D. Stefano, Geophysical modeling via simultaneous joint inversion of seismic, gravity, and electromagnetic data: Application to prestack depth imaging, The Leading Edge (2007) 326–331.

P. G. Lelièvre, C. G. Farquharson, C. A. Hurich, Joint inversion of seismic traveltimes and gravity data on unstructured grids with applications to mineral exploration, in: SEG Technical Program Expanded Abstracts, Denver, USA, vol. 25, 1758–1762, 2010.

L. Nielsen, B. H. Jacobsen, Integrated gravity and wide-angle seismic inversion for two-dimensional crustal modelling, Geophysical Journal International 140 (2000) 222–232.

G. M. Hoversten, F. Cassassuce, E. Gasperikova, G. A. Newman, J. Chen, Y. Rubin, Z. Hou, D. Vasco, Direct reservoir parameter estimation using joint inversion of marine seismic AVA and CSEM data, Geophysics 71 (2006) C1–C13.

P. Dell'Aversana, G. Beransconi, F. Miotti, D. Rovetta, Joint inversion of rock properties from sonic, resistivity and density well-log measurements, Geophysical Prospecting 59 (2011) 1144–1154.

N. Juhojuntti, J. Kamm, Joint inversion of seismic refraction and resistivity data using layered models - Applications to groundwater investigations, Geophysics 80 (2015) EN43–EN55.

J. Sun, Y. Li, A general framework for joint inversion with petrophysical information as constraints, in: SEG Technical Program Expanded Abstracts, Houston, USA, 2013.

P. Podvin, I. Lecomte, Finite-difference computation of traveltimes in very contrasted velocity models: A massively approach and its associated tools, Geophysical Journal International 105 (1991) 271–284.

D. F. Aldridge, D. W. Oldenburg, Two-dimensional inversion with finite-difference traveltimes, Journal of Seismic Exploration 2 (1993) 257–274.

G. W. Bear, H. J. Al-Shukri, A. J. Rudman, Linear inversion of gravity data for 3-D density distributions, Geophysics 60 (1995) 1354–1364.

P. E. Wannamaker, J. A. Stodt, L. Rijo, A stable finite element solution for two-dimensional magnetotelluric modelling, Geophys. J. R. astr. Soc. 88 (1987) 277–296.

J. Nocedal, S. Wright, Numerical Optimization, Springer, second edition edn., 2006.

C. C. Paige, M. A. Saunders, LSQR: An Algorithm for Sparse Linear Equations and Sparse Least Squares, ACM Transactions on Mathematical Software 8.

C. J. Ammon, J. E. Vidale, Tomography without rays, Bulletin of the Seismological Society of America 83 (1993) 509–528.

J. J. Moré, D. Thuente, Line search algorithms with guaranteed sufficient decrease, ACM Transactions on Mathematical Software 20 (1994) 286–307.

J. MacCarthy, B.Borchers, R. Aster, Efficient stochastic estimation of the model resolution matrix diagonal and generalized cross-validation for large geophysical inverse problems., Journal of Geophysical Research 116 (2011) B10304.

C. Bekas, E. Kokiopoulou, Y. Saad, An estimator for the diagonal of a matrix, Applied Numerical Mathematics 57 (2007) 1214 – 1229.

S. Constable, R. Parker, C. Constable, Occam's inversion: a practical algorithm for generating smooth models from electromagnetic sounding data, Geophysics 52 (1987) 289–300.

C. de Groot-Hedlin, S. Constable, Occam's inversion to generate smooth, two-dimensional models for magnetotelluric data, Geophysics 55 (1990) 1613–1624.

F. Martini, R. Hobbs, C. Bean, R. Single, A complex 3D volume for sub-basalt imaging, first break 23 (2005) 41–51.

G. W. Purnell, Imaging beneath a high-velocity layer using converted waves, Geophysics 57 (1992) 1444–1452.

M. M. Fliedner, R. S. White, Depth imaging of basalt flows in the Faeroe-Shetland Basin, Geophysical Journal International 152 (2003) 353–371.

S. Hautot, R. T. Single, J. Watson, N. Harrop, D. A. Jerram, P. Tarits, K. Whaler, G. Dawes, 3-D magnetotelluric inversion and model validation with gravity data for the investigation of flood basalts and associated volcanic rifted margins, Geophysical Journal International 170 (2007) 1418–1430.

M. Panzner, W. W. Weibull, J. P. Morten, Sub-basalt imaging in the Faroe-Shetland Basin using CSEM&MT data to constrain the velocity model, in: SEG Technical Program Expanded Abstracts, Denver, USA, 2014.

G. Hoversten, D. Myer, K. Key, D. Alumbaugh, O. Hermann, R. Hobbet, Field test of sub-basalt hydrocarbon exploration with marine controlled source electromagnetic and magnetotelluric data, Geophysical Prospecting 63 (2015) 1284–1310.

B. Heincke, M. Jegen, R. W. Hobbs, Joint inversion of MT, gravity and seismic data applied to sub-basalt imaging, in: SEG Technical Program Expanded Abstracts, New Orleans, USA, vol. 25, 784–789, 2006.

D. Colombo, M. Mantovani, S. Hallinan, M. Virgilio, Sub-basalt depth imaging using simultaneous joint inversion of seismic and electromagnetic (MT)

data: a CRB field study, in: SEG Technical Program Expanded Abstracts, Las Vegas, USA, vol. 27, 2674–2678, 2008.

A. Manglik, S. K. Verma, K. H. Singh, Detection of sub-basaltic sediments by a multi-parametric joint inversion approach, Journal of Earth System Science 118 (2009) 551–562.

M. D. Jegen, R. W. Hobbs, P. Tarits, A. Chave, Joint inversion of marine magnetotelluric and gravity data incorporating seismic constraints: Preliminary results of sub-basalt imaging off the Faroe Shelf, Earth and Planetary Science Letters 282 (2009) 47–55.

P. Tarits, Algorithme de modlisation magntotelluric en deux dimension, Ph.D. thesis, IPG, Paris, France, 1984.

R. S. White, J. R. Smallwood, M. M. Fliedner, B. Boslaugh, J. Maresh, J. Fruehn, Imaging and regional distribution of basalt flows in the Faroe-Shetland Basin, Geophysical Prospecting 51 (2003) 215–231.

J. Gallagher, P. Dromgoole, Exploring below the basalt, offshore Faeroes: a case history of sub-basalt imaging, Petroleum Geoscience 13 (2007) 213–225.

J. Schuler, P. A. F. Christie, R. S. White, Seismic Attenuation of Flood Basalts in the Brugdan and William Wells and stratigraphic Correlation on the Faeroe Shelf, EAGE 74th Conference & Exhibition, Copenhagen, Denmark .

O. Dubrule, Geostatistics for seismic data integration in earth models, Distinguished Instructior Series No.6., EAGE, Distinguished Instructior Series No.6., 2003.

R. Spitzer, R. S. White, P. A. F. Christie, Enhancing subbasalt reflections using parabolic Tau-p transformation, The Leading Edge (2003) 1184 – 1201.